Streamflow monitoring at high temporal resolution based on non-contact instruments in a river prone to bathymetric shifts

G. Nord[1], S. Safdar[2], M. Hasanyar[3], K. O. Eze[1,4], R. Biron[1], G. Freche[1], H. Denis[1], C. Legout[1], A. Hauet[1], and M. Esteves[1]

[1] Univ. Grenoble Alpes, CNRS, IRD, INRAE, Grenoble INP, IGE, F-38000, Grenoble, France

[2] Department of Civil and Environmental Engineering, University of Vermont, USA

[3] 3D EAU - Groupe Alcom, 75013, Paris, France

[4] Institute for hydraulic Engineering and Water resources management, TUWien, Austria

Corresponding author: Guillaume Nord (guillaume.nord@univ-grenoble-alpes.fr)

Key Points:

- A streamflow monitoring method combining water level radar, surface velocity radar, imagery and topographic surveys is presented
- A single proportional relation, resistant to bathymetric changes, is established between maximum surface velocity and bulk velocity
- Theoretical models predict the relation between maximum surface velocity and bulk velocity and the position of the maximum surface velocity

Abstract

This study presents a reliable methodology for monitoring streamflow in a dynamic river of the Alps prone to bathymetric changes using non-contact instruments. The method relies on water level and surface velocity radar monitoring, discharge measurements by Large-Scale Particle Image Velocimetry (LSPIV), and topographic surveys. A single proportional relation, resistant to bathymetric changes, is established between maximum surface velocity ($V_{s,max}$) and bulk velocity (U_{mean}). Different methods are used to build this relation: (i) an empirical approach calibrated with the LSPIV measurements; (ii) the Isovel model; (iii) the Q-Commander software developed by the Sommer company. The applicability of the method is tested over a 2.5-year dataset. Compared to the empirical approach, both models, which require minimal input data, predict well the $V_{s,max}$-U_{mean} relation. The location of the maximum surface velocity, which reveals to be resistant to bathymetric changes, is also well predicted by these models. Discharge is calculated at a time step of 10 min by multiplying the bulk velocity and the wetted area. The results are compared to the discharge series at the historical station located 2.5 km further upstream, which has a stage-discharge rating curve. Good agreement is observed when surface velocity is above 0.7 m/s, but accuracy decreases for lower velocities. A simplified uncertainty analysis estimates a 20% relative error on discharge calculated with the presented method.

Plain Language Summary

Small rivers are very densely distributed over the world, yet only a few are monitored. Many small rivers are located in mountainous areas and are potentially subject to flash floods and geomorphological processes. The aim of this study is to propose a monitoring method adapted to these environments, with high temporal resolution (~ 10 min) and non-contact instruments (water level and surface velocity radars, video camera), able to give a simple and direct access to the discharge in order to reduce operating costs and make possible to equip many more small rivers in the future. This approach is tested in a river of the Southern Pre-Alps in France. A linear relation is determined empirically between the maximum surface velocity (Vs,max) and the average velocity of the cross-section (Umean) using image analysis of videos recorded during floods. This relation is resistant to morphological changes and the position of the maximum surface velocity remains stable over time. The discharge time series is calculated by multiplying Umean, derived from the Vs,max-Umean relation (with the radar velocity assimilated to Vs,max), and the wetted cross-section, derived from the water level radar. The results are validated through comparison with a reference station on the same river.

1 Introduction

Many applications require monitoring of discharge in rivers, both in the operational field (e.g. flood and drought warning systems, water resource management, hydroelectric production) and in academic research (e.g. hydrological modelling, calculation of flux of sediment, nutrient or contaminant). Streamflow monitoring networks are very unevenly distributed around the world. They are mainly located in developed countries, often managed by federal or governmental agencies and generally concern rivers with a drainage area greater than 100 km². The United States of America (USA) is certainly the best equipped country in the world with a network of more than 8000 stations belonging to the National Streamflow Network (NSN) managed by the United States Geological Survey (USGS) (Eberts et al. 2018). These stations cover drainage

areas ranging from 0.08 km² to 253000 km². The median drainage area is 295 km²; 96.7% (resp. 71.7%) of the stations cover drainage areas larger than 10 km² (resp. 100 km²). In contrast, the southern countries have a severe lack of streamflow monitoring stations. Satellite observation (e.g. SWOT) will make it possible to improve the situation for the world's major rivers, which are more than 100 m wide, or even 50 m wide in the best case, by providing hydrometric data at a maximum frequency of 21 days (Rodrigez et al., 2020). However, the issue of rivers covering drainage areas of less than 100 km², referred to as small rivers in this study, will not be improved by satellite observation in the next decade although they represent an incalculable number of watercourses. In addition, at this scale, observation has to be done at a high temporal resolution (sub-hourly) due to the dynamics of the hydrosystems, so in situ monitoring will remain the rule for a while. Recent studies, such as on land carbon budget to give just one example (Duvert, 2018; Botter, 2022), showed the need to increase the density of streamflow monitoring in small rivers. The question is how to proceed, bearing in mind that current approaches cannot be applied because of the considerable resources (human, equipment) they involved. Therefore it is particularly important for the scientific community to contribute to the development of new monitoring approaches, using parsimonious and reliable methodologies.

Techniques and methods for reference discharge measurement obtained at a specific time (so-called gauging), enabling to measure directly the discharge, have considerably evolved in the last decades. It is now possible to measure reference discharge with a known level of uncertainty in a wide range of conditions of river size, slope and hydrological conditions. In small rivers, impeller, electromagnetic and acoustic current meters as well as dilution methods are the most commonly tools used for low to medium flow conditions. For high flow conditions, the use of imagery like LSPIV (Muste et al., 2008) or STIV (Fujita et al., 2007) and portable surface velocity radar (Welber et al. ,2016) has enabled measurements in situations never explored before.

In contrast, streamflow monitoring require specific approaches compared to the reference discharge measurements. The conventional hydrometric approach still remains the most commonly used approach to date. It combines water level monitoring and the establishment of a stage-discharge (H-Q) rating curve allowing the water level time series to be posteriori converted to streamflow time series. It has incontestable advantages: i) the low cost and high accuracy of equipment for water level monitoring, ii) the quality of streamflow time series when reference discharge measurements are carried out regularly (roughly 10 times per year), iii) the availability of methods for estimating uncertainties such as the Bayesian rating curve framework (Le Coz et al., 2014) or LOWESS regression (Coxon et al., 2015), see Kiang et al. (2018) for a review. On the other hand, the drawbacks of this method are: i) the operational costs due to the human resources involved , ii) the diversity of technical equipment required for the reference discharge measurements, iii) the initial delay in the provision of streamflow time series as it might take several years before establishing a reliable H-Q rating curve based on an extended range of reference discharge measurements, iv) the exposure to hydro-meteorological risks for the staff carrying out reference discharge measurements during floods, v) the sensitivity to hydraulic control shifts, mainly caused by changes in bathymetry. Indeed, as soon as a flood significantly modifies the geometry of the cross-section (deposition or erosion), the H-Q rating curve has to be completely rebuilt with a new set of reference discharge measurements. In highly morphogenic rivers, it is even impossible to apply this approach as the H-Q rating curves change so often.

Since the 2000s, other approaches have gradually been developed. They can be grouped together under the heading of velocimetric approaches insofar as they combine both the monitoring of the water level (H) and the velocity (V) at high temporal resolution. A first attempt has been to automate image-based discharge measurement techniques from one or more fixed cameras (Hauet et al., 2008; Le Coz et al., 2010; Stumpf et al., 2016; Li et al., 2019). Water level may be monitored by the camera itself or by an independent instrument (e.g. pressure sensor, radar, ultra sound). Video sequences of a few seconds are recorded at high temporal resolution (e.g. every 5 to 30 minutes). Surface velocity fields are then calculated usually in real time on site to avoid the need for extensive data transfer and storage. There exist commercial solutions for such technology (e.g. Tenevia, Vortex-IO, Seba's Discharge Keeper, Xylem's Q-Cam) which are either connected to the grid or autonomous in energy. Another velocimetric approach which has seen moderate growth over the last decade is the index velocity method. It was initially presented by Levesque and Oberg (2012). This approach can substitute completely the conventional hydrometric approach for the production of discharge time series (Kästner et al., 2018; Gonçalves et al., 2023). It requires two relations: (i) a H-A_{wet} relation for the calculation of the wetted area (A_{wet}) based on regular topographical surveys of the monitored cross-section; (ii) a V-U_{mean} relation for the calculation of the mean cross-section velocity U_{mean} (so-called bulk velocity). The V-U_{mean} relation, calibrated using a set of reference discharge measurements, can be a simple-linear regression, a compound-linear regression or a multiple-linear regression (Levesque and Oberg, 2012). Once the H-A_{wet} and V-U_{mean} relations are built, the calculation of discharge at any time step (t) can be done by multiplying the terms $A_{wet}(t)$ and $U_{mean}(t)$. The index velocity (V) can be monitored using different types of instruments (e.g. horizontally-oriented Acoustic Doppler Current Profiler, ultrasonic transit-time, surface velocity radar, acoustic Doppler velocimeter), which makes this approach very flexible. However, the main limitations of this approach are: (i) it still requires a large number of reference discharge measurements, which implies both operating costs and human resources; (ii) velocity monitoring is generally not as accurate as water level monitoring, which introduces noise in the calculated discharges; (iii) it still needs regular survey of the bathymetry of the cross-section, to establish and maintain the H-A_{wet} relation.

The aim of this study is to produce continuous time series of discharge focusing on steep rivers (slope typically higher than 1%), subject to frequent topographic changes due to morphogenic floods, where none of the above approaches are really suitable. The use of non-contact instrumentation is preferred in order to avoid problems of maintenance and destruction by flash floods. Such conditions are common in mountainous regions of Mediterranean and tropical areas, where discharge may vary up to 3 or 4 orders of magnitude in a few hours. We propose to follow a velocimetric approach, similar to the index velocity method, using a local surface velocity monitored by a fixed radar (V_s). We propose to establish a V_s-U_{mean} relation based on reduced information, i.e. topographic surveys and automatic video recordings, which can be obtained outside flood periods for the former, and during flood periods for the latter. Specifically, we decide to focus on the $V_{s,max}$-U_{mean} relation between the maximum surface velocity and the bulk velocity. There are two reasons for this choice: (i) Chiu (1988, 1991) and Chiu and Said (1995) identified a linear relation between U_{mean} and the maximum velocity V_{max} in a river cross-section, with this relation invariant with time and discharge (Chiu and Tung, 2002; Chiu and Chen, 2003). The existence of this linear relation was verified by Moramarco and Singh (2010) and Fulton et al. (2020) with observed data. (ii) The vertical axis on which V_{max} occurs is called the "y axis". $V_{s,max}$ is located in the same vertical axis as V_{max} as demonstrated by Chen and Chiu

(2004) and Fulton et al., (2020). In natural river sections controlled by slope and roughness, it seems reasonable to assume that V_{max} is located close to the surface and therefore $V_{s,max}$ can be a good approximation of V_{max}.

A new dataset of observed data collected in a river of the southern French pre-Alps is used to apply this framework. The first objective of this study is to verify the existence of a linear $V_{s,max}$-U_{mean} relation using image-based surface velocity and discharge measurements derived from automatic video records and regular topographic surveys. Additionnaly, the resistance of this relation to morphological changes is tested. The second objective is to test if this linear $V_{s,max}$-U_{mean} relation can be reasonably well predicted by theoretical models. Such models include: (i) the isovel model, initially developed by Maghrebi, (2006), which is a theoretical model based on an analogy from Biot-Savart's law of electromagnetism (Hayt, 1981) to calculate the distribution of velocity within a cross-section, (ii) the Q-Commander software developed by the Sommer company (Sommer, 2013). The third objective is to test the steadiness of the localisation of the maximum surface velocity within the cross-section using image-based surface velocity measurements and theoretical models regardless of the existence of morphological changes. The fourth objective is to evaluate the ability to produce streamflow times series using the framework defined by the index velocity method and the $V_{s,max}$-U_{mean} relation predicted by the empirical method calibrated with image-based results.

2 Materials and Methods

2.1 Site description and monitoring equipment

This study is based on data collected in the Galabre river which belongs to the Draix-Bléone Observatory (https://oredraixbleone.inrae.fr/en/) and is part of the French research infrastructure OZCAR (Gaillardet et al., 2018). The Galabre river is a tributary of the Bléone river. The Galabre catchment is presented in detail by Esteves et al. (2019) and Legout et al. (2021). Mean annual rainfall is respectively 958 mm at La Robine sur Galabre close to the outlet (alt. 750m a.s.l) and 1046 mm at Ainac in the upstream part of the catchment (alt. 1145m a.s.l.). Erosion and sediment transport processes are very active in this catchment due to the presence of patches of non-vegetated badlands (representing 9% of the total area), the general slope of the basin (mean slopes of 54, 19 and 6% for hillslopes, intermittent rivers and the main river, respectively) and the influence of Mediterranean rainfall and mountain thunderstorms (Esteves et al., 2019).

A conventional hydrometric station monitors streamflow at a 10-min time step at La Robine sur Galabre, at the outlet of the 20 km² catchment, since 2007 (Legout et al., 2021). The cross-section is very stable as, in this reach, the river flows over limestone slabs and the local slope (3 %) is high enough to prevent sediment deposition. The station is equipped with a radar for water level monitoring. A stage-discharge rating curve was established from 35 reference discharge measurements using different gauging techniques (dilution, impeller current meter, electromagnetic current meter) applied between 2007 and 2014 (ranging from 0.017 $m^3 s^{-1}$ to 0.948 $m^3 s^{-1}$) and an extrapolation performed by hydraulic modelling (HEC-RAS) (Esteves et al., 2019).

A new station called RIPLE (River Platform for Monitoring Erosion) was installed in October 2018 on the Galabre river, 2.5 km downstream of La Robine sur Galabre. Nord et al. (2020) presented the developpement of the RIPLE platform, an autonomous low-power instrument

platform for monitoring water and solid discharges in mesoscale rivers. The RIPLE station is equipped with a fixed surface velocity radar (so-called V radar), a water level radar (so-called H radar) and a video camera dedicated to Large Scale Particle Image Velocimetry (LSPIV) analysis as illustrated by the schematic diagram in Figure 1. A staff level gauge is also installed on the river bank. Both radars are installed on the same extension arm anchored to the vertical wall of the bridge on the downstream side, as shown in Figure 2. The sampling time step of the platform is 10 min. Water level and surface velocity data are remotely transmitted once a day to the lab in Grenoble. The RIPLE station is located in a gravel-bed river reach prone to frequent bathymetry changes.

The H radar (CRUZOE manufactured by Paratronic) works on the time-of-flight principle. It points vertically below its position with a total opening angle of 12°. Each logged value is the average of three measuring cycles, each lasting 4 s and separated by 5 s. During each measuring cycle, the instrument makes 16 measurements per second. The logged variable is called H_{rad} in this study. The standard deviation (STD) is also logged simultaneously.

The V radar (RG-30 manufactured by Sommer) works on the Doppler principle. For more details about the radar Doppler technology, the readers can refer to the study presented by Fulton et al. (2020), Son et al. (2023) and Huang et al. (2023). The V radar points slightly further downstream at an angle of 32 degrees to the vertical and with a total opening angle of 12°, so that the centre of the zone targeted by the V radar is located 3.7 m further downstream for very low flow conditions (respectively 2.5 m further downstreal for a water depth of 2 m). Every measurement is time averaged over 30 records obtained at a frequency of 1 Hz. The logged variable is called V_{rad} in this study.

The AXIS P1435-LE camera is mounted on a mast from the bridge deck, looking downstream. The camera, which is triggered when the value of water level exceeds a threshold, records video at an interval of 30 min during storm events. It takes short videos (approximately 7 s) of the river scene at a rate of 30 frames per second. This configuration allows for effective utilization of media storage, reduces energy consumption of the platform and ensures that only high flow conditions are captured for LSPIV analysis. The video sequences stored in a SD card of the LSPIV camera are retrieved regularly during field visits.

The LSPIV cross-section used for analysis and calculation is located slightly further downstream of the bridge. Indeed, the presence of a natural step formed by the bedrock under the upper part of the bridge creates a hydraulic jump and conditions that are particularly challenging for hydrometric monitoring. The river is more uniform downstream of the bridge, and therefore more appropriate to velocity exploration. The horizontal distance between the H radar and the "LSPIV cross-section" shown in Figure 2 is approximately 10 m. The slope of the river is of the order of 2% in this reach, which means that, assuming a slope of the free surface parallel to the slope of the bed, a drop in the water level of 0.2 m is applied to the value of H_{rad} to obtain the corresponding value in the "LSPIV cross-section", so-called H_{LSPIV}.

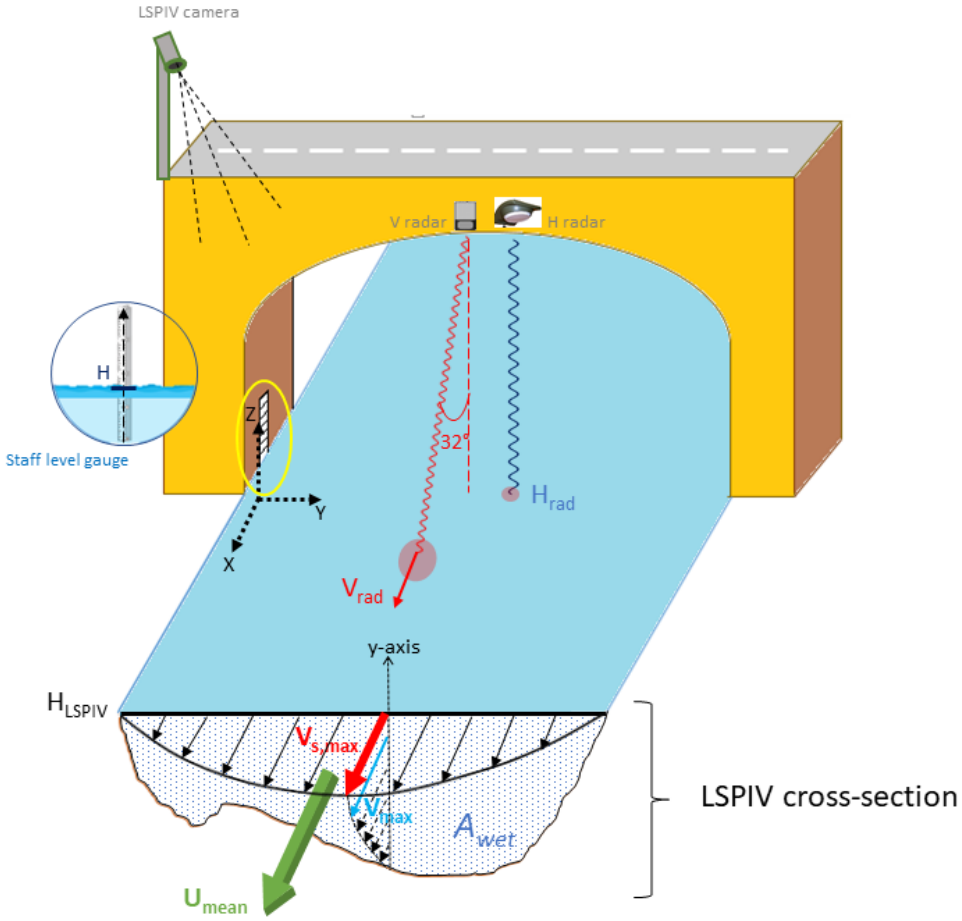

Figure 1 – Conceptual sketch of a velocimetric station with the different instruments deployed including fixed surface velocity radar (V radar), water level radar (H radar), LSPIV camera and staff level gauge.

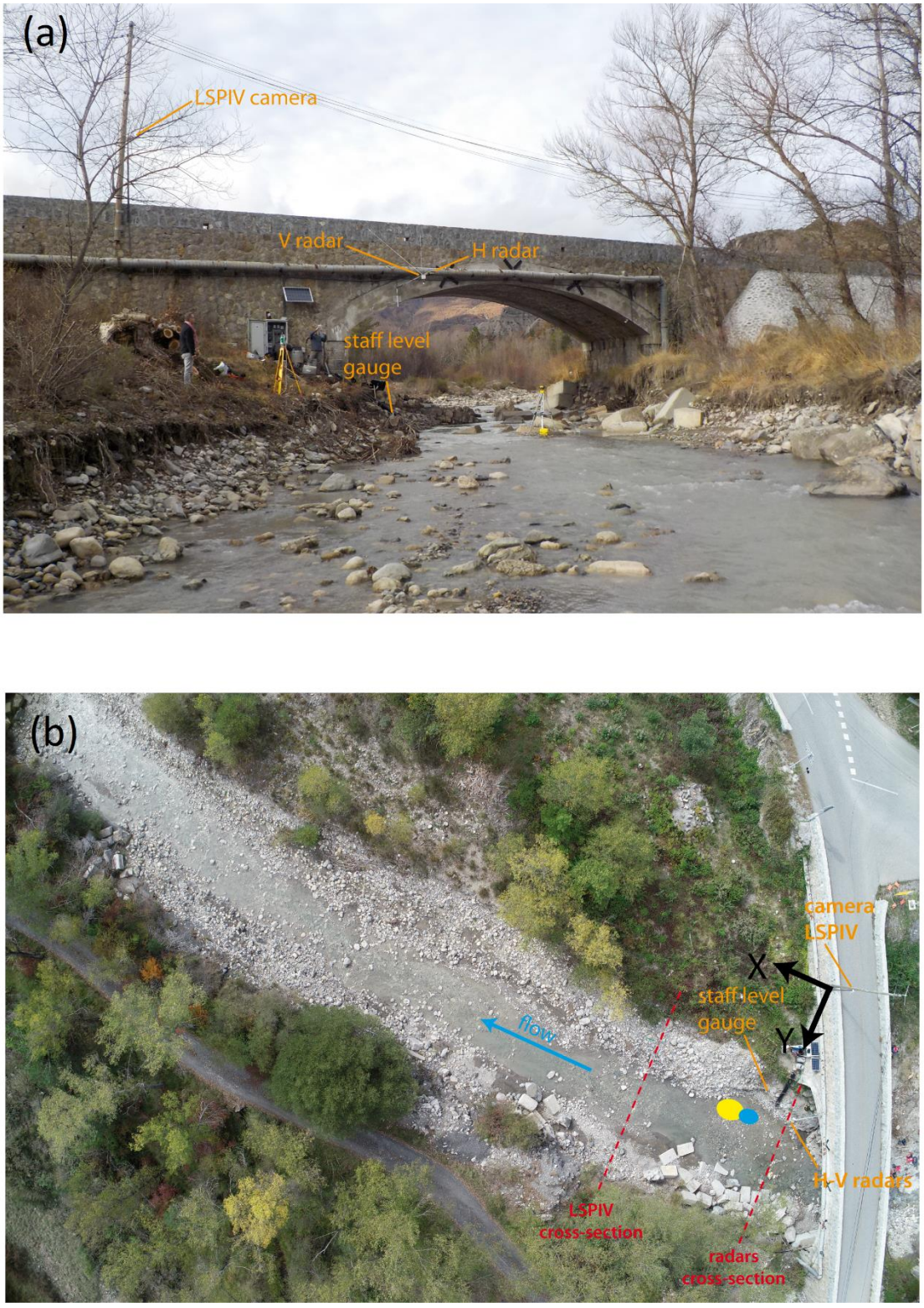

Figure 2 - a) photograph of the RIPLE platform on the Galabre River taken from downstream of the bridge and looking upstream, b) aerial view of the bridge housing the RIPLE platform and the river reach downstream of the bridge with the radars cross-section, the LSPIV cross-section, and the location of the instruments. The yellow ellipse indicates the approximative area targeted by the V radar in low flow conditions such as those shown in the image. The blue ellipse indicates the approximative area targeted by the V radar when the water depth is around 2 m.

2.2 Data control and curation

The period from October 2018 to May 2021 is considered in this study. For the upstream station at La Robine sur Galabre, data are regularly controlled before being publicly released through the online data platform of the Draix-Bléone observatory (https://bdoh.irstea.fr/DRAIX/nos-donnees?site=Galabre). The quality codes are presented in Table 1. The raw data produced by the H radar are often of good quality and directly validated.

For the downstream station, the same procedure of quality control is applied. Quality codes are assigned to processed data as presented in Table 1. Velocity data are often more spurious than water level data (Blake and Packman, 2008; Nord et al., 2014; Fulton et al., 2020; Rahman Khan et al. 2021). Customized filters based on statistical parameters have been designed for surface velocity data. The methodology is adapted from Blake and Packman (2008) and Nord et al. (2014). The order of filters follows the same sequence:

1. Missing values (NaN): values are replaced by -9999 and quality code ‘l’ is assigned. Given the regular morphological changes in the river bed, some periods of missing data occur due to the presence of a gravel bar that formed temporarily below the H-V radars on the right bank of the river. This situation represents 34.2% of the total dataset and is rather more frequent from the end of 2020.

2. Repeat velocity error: Given natural flow variability and resolution of radar, more than three repeated and consecutive values are unlikely. These are clone observations and are replaced by -9999 with a quality code ‘i’.

3. Spurious observations: A moving window average is used with a fixed window size of 4 steps (40 min). The observation is considered erroneous when difference between recorded and moving average at a time step is more than 30%. These are replaced by -9999 and quality code ‘i’ is assigned.

4. Physical and configuration limit: The maximum surface velocity in natural river is limited to 7.0 m/s. The lower limit of 0.2 m/s is recommended by manufacturer. The observations exceeding maximum and below minimum are replaced by -9999 and quality code ‘i’ is assigned.

5. Signal to noise ratio (SNR): The radar manufacturer recommends a lower limit for the value of the quality. The data with a SNR value lower than 30 is replaced by quality code ‘d’. The values are maintained since deleting these may lead to parting away of useful information during subsequent analysis.

6. Valid: All other remaining logged data is checked and quality code ‘v’ is assigned. This represents 51.2% of the total dataset and 77.8% of the dataset without missing data. Most of unvalidated data are associated with low velocities values, typically lower than 0.5 m/s.

283 **Table 1 – Quality codes assigned to processed data**

Sr.No.	Quality	Code	Value	Comment
1	Valid	v	raw data	observation found valid
2	Doubtful	d	raw data	unexpected observation but still physically acceptable
3	Estimate	e	reconstructed	reconstructed data (e.g. interpolation)
4	Lack	l	-9999	gap - missing observation (blank or NaN)
5	Invalid	i	-9999	erroneous observation that has been deleted

284

2.3 Topographic surveys and detection of bathymetric shifts

As seen in Figure 2, the downstream station (RIPLE) is located in a gravel-bed river reach where the morphology is likely to change regularly due to active sediment transport processes. Different methods, i.e. total station, lasermeter, D-GPS, are used to carry out topographic/bathymetric surveys of the LSPIV cross-section as illustrated in Figure 2. Each time, three reference points are surveyed in order to convert all the data into the same local reference frame represented in Figures 1 and 2.

A first survey of the LSPIV cross-section was conducted in October 2018 when the station was installed. Regular surveys were then carried out during field visits (9 in total over the study period). These data enable to build the H-A_{wet} relation of the LSPIV cross-section after each new bathymetric change. Plotting the H-V data provided by the H-V radars can help detect bathymetric changes (Rahman Khan et al., 2021). Indeed, a sudden shift in the H-V scatter plot, which often occurs during major floods, indicates a change in bathymetry and the need for a new bathymetric survey of the LSPIV cross-section. Points that cause the deviation in the scatter plot can reveal the exact timing of the morphological changes. By following this procedure, it is possible to accurately track and identify the changes occurring in the bathymetry. The AreaComp version 2.1 software (United States Geological Survey, 2021) was used to calculate the H-A_{wet} relations.

2.4 LSPIV analysis

Large scale particle image velocimetry (LSPIV) is a technique that performs image processing and pattern tracking to measure the velocity of a flowing fluid (Hauet et al., 2008; Muste et al., 2008; Le Coz et al., 2010). It works by analysing consecutive images taken at a fixed time interval and tracking the movement of visible patterns at the surface of the fluid thanks to a pattern-matching algorithm, with a likelihood criterion based on cross-correlation. In this study, the software Fudaa-LSPIV v1.8.2 (Le Coz et al. 2014) was used. Figure 3 illustrates the various steps involved in producing a surface velocity field and calculating discharge.

Step 1 – Image Extraction: A total of 2381 video sequences were recorded during the study period. However, 2024 video sequences were withdrawn due to improper camera trigger settings between 04/10/2018 and 03/07/2019. In addition, all video sequences recorded at night and with bad quality of tracers were omitted as they were not exploitable for the LSPIV. In the end, a total of 69 video sequences were selected for this study. Once video sequences were selected manually, images were extracted using default time step of 0.033 s. The value of the water level in the "LSPIV cross-section", H_{LSPIV}, was also entered for each video sequence.

Step 2 – Orthorectification: the coordinates of 11 ground reference points marked on site at different locations using black and white paint were used for orthorectification. This step allows to calibrate the camera model, to correct distortion due to perspective and provides metric scale to images instead of pixels. A resolution of 0.02 m/pixel was assigned for good visualization of natural tracer.

Step 3 – LSPIV analysis: Pearce et al. (2020), evaluated application of various image velocimetry algorithms, including the widely used LSPIV algorithm. They found that velocity results are sensitive to the interrogation area (IA) parameter. Le Coz et al. (2010) recommended that IA be sized enough to include enough tracers and small enough to be computationally effective. Therefore, the value of IA was derived from a first test involving two video sequences covering a wide range of surface velocities, i.e. the video sequence corresponding to the highest measured radar velocity and the video sequence corresponding to the lowest radar velocity. This methodology assured the applicability of a single parameter choice for the entire range of video sequences. The value of IA was set to 0.48 m. The spatial resolution of the grid used to perform LSPIV calculation was 0.36 m in the Y direction and 0.66 m in the X direction. There were 40 points in the Y direction covering the width of the river at high flows and 30 points in the X direction from X = 2 m to X = 17.65 m.

Step 4 – Post processing: Instantaneous velocities obtained for each pair of consecutive images were used to calculate time-averaged results of surface velocity field over the whole video sequence. This was carried out after applying filters on minimum and maximum correlation coefficient and velocity. In this study, correlation range of 0.6-1.0 and minimum velocity of 0.5 m/s were found to be the most suitable filters to remove spurious results and obtain the most relevant surface velocity fields.

Step 5 – Discharge and $V_{s,max}$: The cross-section where the discharge is to be measured (so-called "LSPIV cross-section") was imported. This transect was interpolated at a regular step of 0.1 m with calculation of the corresponding water depth at each new point. The search radius was 1 m in the longitudinal direction and 0.2 m in the transverse direction. This means that the points of the grid that are within this search radius are weight-averaged by distance to produce the velocity component perpendicular to the transect at each interpolated point of the transect. Fudaa-LSPIV uses a velocity index (α), so-called depth-averaged to surface velocity ratio, to transform surface velocity to depth-averaged velocity. Welber et al. (2016), Hauet et al. (2018) confirmed the acceptability of default velocity index value of 0.85 on multiple sites under different hydraulic configurations. The default value of 0.85 was used in this study since no ADCP or current meter measurement was available to adjust the value of α. Discharge was then computed as the sum of the contributions of discharge per unit width over the whole interpolated transect. Finally, the maximum value of surface velocity (so-called V_{s,max_LSPIV}) as well as its spatial coordinates were extracted by calculating the moving average over 8 points to smooth out any erratic results.

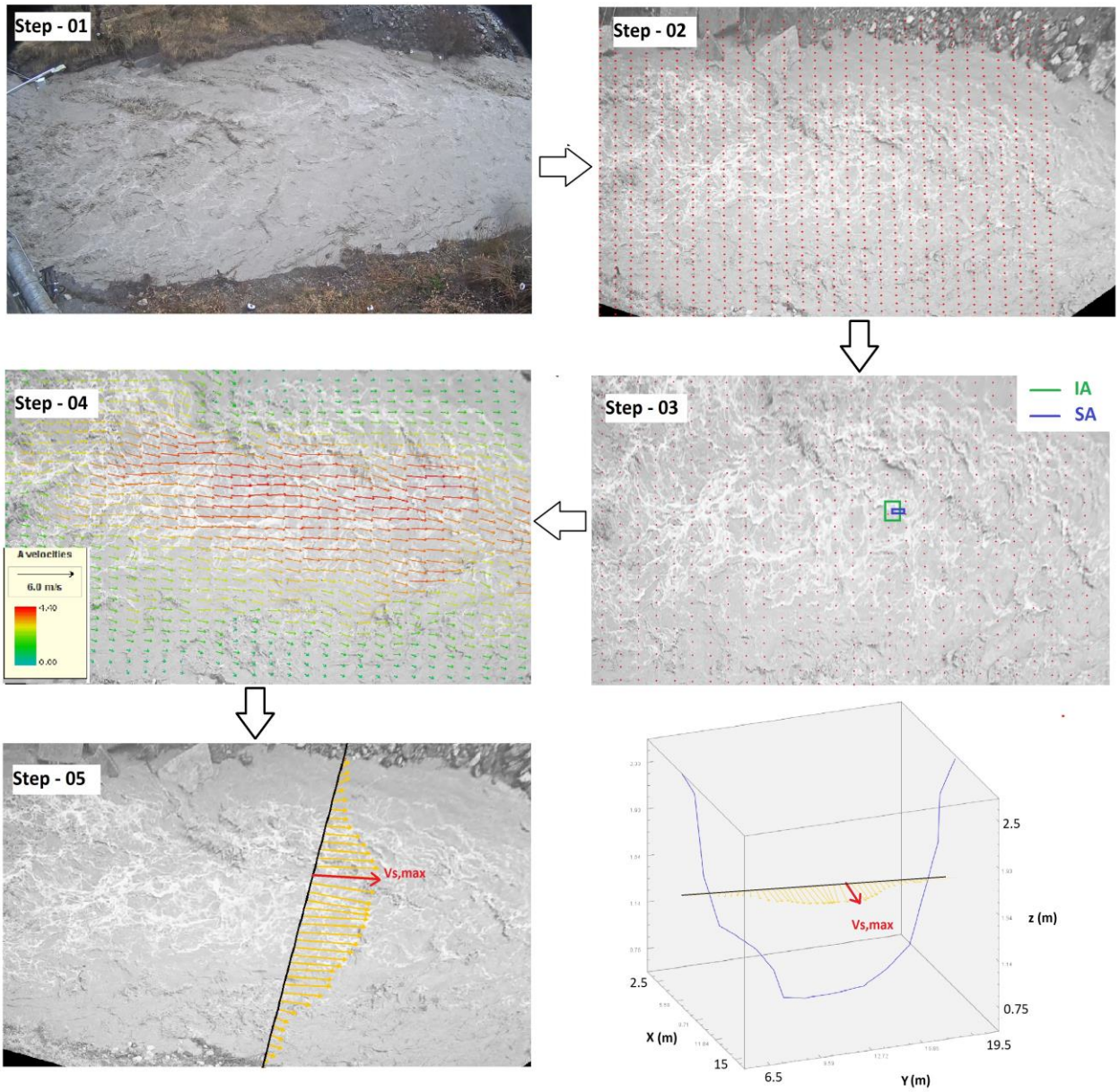

Figure 3 – Main steps involved in producing surface velocity field and calculating discharge using Fudaa-LSPIV v1.8.2

2.5 The V_{s,max_LSPIV}-U_{mean} relation

Four methods were initially identified to build the $V_{s,max}$-U_{mean} relation : (i) the Entropy model; (ii) the Isovel model; (iii) a calibration using LSPIV measurements; (iv) the Q-Commander model. However, the application of the Entropy model was not concluding in our case and the results were excluded from the study. Given the importance of this approach in the literature, the Entropy model is still presented briefly below since part of its formalism has been retained for this study. The possible reasons why the application failed are also mentioned.

2.5.1 Entropy model

Chiu (1987, 1988), Chiu and Tung (2002), Chiu and Chen (2003) proposed a velocity distribution equation based on the probability concept and the Shannon's information entropy (Shannon, 1948). The velocity distribution at the "y axis", i.e. the axis of the cross-section on which the maximum velocity V_{max} occurs, is represented by:

$$u = \frac{V_{max}}{M} ln[1 + (e^M - 1)F(u)] \quad (1)$$

where u = velocity as a function of depth at the "y axis"; V_{max} = maximum velocity at the "y axis"; M = parameter of the probability distribution used to describe the velocity distribution; and $F(u) = \int_0^u f(u)\,du$, which represents the cumulative distribution function, or the probability of a randomly sampled point velocity that is less than or equal to u.

The probability distribution $f(u)$, is resilient and is invariant with time and water level at a channel cross section. M is constant at a channel cross section. Chiu (1987, 1988) identified a linear relationship, function of the parameter M, between U_{mean} and V_{max} in a channel cross-section. $\emptyset$, which is the ratio between U_{mean} and V_{max} is expressed by Chiu and Tung (2002), as follows:

$$\emptyset = \frac{U_{mean}}{V_{max}} = \frac{e^M}{(e^M - 1)} - \frac{1}{M} \quad (2)$$

In its original form, the method requires at least one complete distribution of velocity within the cross-section, obtained by ADCP or current meter for example. Since such data did not exist in our case, the original method as applied by Fulton et al. (2020) could not be applied. Alternatively, Farina et al. (2014) proposed derived procedures applicable to cases where only the surface velocity is available (either the complete surface velocity distribution or only the maximum surface velocity). These derived procedures were attempted in our case using the LSPIV measurements. However, the results were not satisfactory. It seems that the parametric formula used to determine the position of the maximum velocity in the vertical initially proposed by Chiu and Tung (2002) was calibrated with data from large rivers and is not suitable for small rivers.

With reference to the formalism of the Entropy model, we introduce the ratio $\emptyset_s$ between U_{mean} and $V_{s,max}$ expressed as:

$$\emptyset_s = \frac{U_{mean}}{V_{s,max}} \quad (3)$$

2.5.2 Isovel model

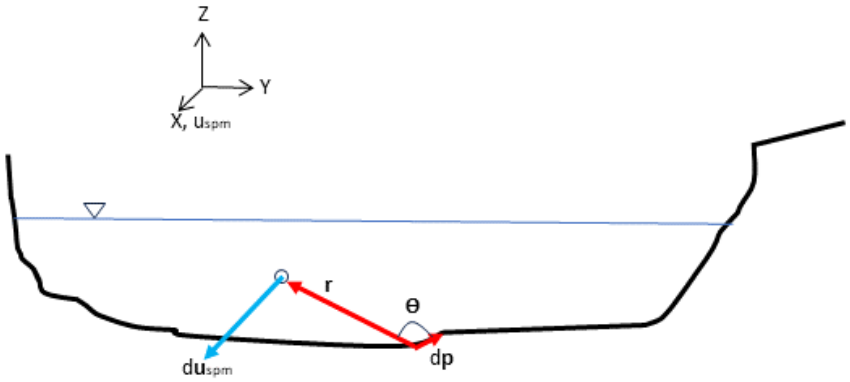

Figure 4 - Section where u_{spm} is calculated for each point inside the cross-section considering a desired mesh size.

The original motivation of the development of the Isovel model was to improve reference discharge measurements by minimising the number of sampling steps during velocity gauging, if possible to a single point velocity measurement. The model was initially developed by Maghrebi (2003). This approach draws its inspiration from the Biot–Savart law (Hayt,1981), which can be used to calculate the intensity of a magnetic field generated at a point in space by an infinitely long wire carrying a stationary and steady current. Maghrebi (2006) used this analogy to quantify the impact of perimeter roughness on velocity inside the channel. In this method, the velocity of any point inside the river cross-section depends on its distance (r) from the wetted perimeter (Pw) and the constant related to the boundary roughness (c_1). u_{spm} means the velocity of a single point measurement. As in Figure 4, the incremental velocity of any point inside the cross-section $\mathbf{du_{spm}}$ is due to cross product between the function f(**r**), an infinitesimal element of wetted perimeter **dp**, and c:

$$\boldsymbol{du_{spm}} = f(\boldsymbol{r}) \times c_1 \, \mathbf{dp} \tag{4}$$

f(r) is the dominant velocity function according to Kavousizadeh and Ahmadi (2018) and Ali and Maghrebi (2023). The direction of the velocity is normal to the plane containing the vector of the infinitesimal element of wetted perimeter (**dp**) and the vector drawn from the infinitesimal element of wetted perimeter to the point where the velocity is calculated (**r**). Since vectors **r** and **dp** are located in a plane normal to the main flow direction, the cross product of them is normal to the plane of the section.

The velocity in the main flow direction can be obtained by integration along the wetted perimeter as:

$$\boldsymbol{u_{spm}} = \int_0^{Pw} \boldsymbol{du_{spm}} = \int_0^{Pw} f(\boldsymbol{r}) \times c_1 \, \mathbf{dp} \tag{5}$$

And the scalar of the velocity in a Cartesian coordinate system (x,y,z), as shown in Figure 4, is obtained as:

$$u_{spm}(\mathrm{y},\mathrm{z}) = \int_0^{Pw} f(r)\, c_1\, dp\, sin\theta = \int_0^{Pw} c_1\, sin\theta\, f(r)\, dp \tag{6}$$

As a result, points far from the perimeter will have higher values of u_{spm} than those which are located close to the perimeter.

Then, for the distance function f(r), Maghrebi (2006) considers power law of velocity distribution function (Chen, 1991) as follows:

$$f(r) = u_*(c_2\, r^{\frac{1}{m}}) \tag{7}$$

Where u_* is the shear velocity which comes from $u_* = \sqrt{\tau_0/\rho}$ with τ_0 the boundary shear stress and ρ the mass density of fluid, c_2 is the coefficient related to turbulent intensity, and m is an exponent ranging between 1/4 to 1/12 which depends on the intensity of the turbulence. Numerous experiments show that a value of m = 1/7 agrees well for turbulent velocity profiles in smooth boundaries (Chen, 1991), (Wright and Parker, 2004).

Then, replacing Equation 7 in Equation 6 gives:

$$u_{spm}(\mathrm{y,z}) = \int_0^{Pw} c_1 u_* \,(c_2\, r^{\frac{1}{m}})\, \sin\theta \, \mathrm{dp} \tag{8}$$

By considering $c = c_1\, c_2\, u_*$ and $m = 7$, Equation 8 can be rewritten as:

$$u_{spm}(\mathrm{y,z}) = \int_0^{Pw} \mathrm{c}\,(r^{\frac{1}{7}})\, \sin\theta \, \mathrm{dp} \tag{9}$$

The bulk theoretical velocity U_{spm} is obtained by integrating u_{spm} over the channel section:

$$U_{spm} = \frac{\int_A u_{spm}(y,z)\, dA}{A} = \frac{\int_A (\int_0^{Pw} c\,(r^{\frac{1}{7}})\, \sin\theta\,)\mathrm{dA}}{A} \tag{9}$$

Finally, dividing the theoretical point velocity to the theoretical bulk velocity provides with the dimensionless isovel coefficient (η) at any point of the cross-section:

$$\eta(y,z) = \frac{u_{spm}(y,z)}{U_{spm}} \tag{10}$$

In case of uniform roughness and shear velocity along the perimeter, the term c is cancelled and Equation 10 only depends on r, θ and dA. This assumption was made in this study as it was done in the work of Kavousizadeh and Ahmadi (2018). This results in a parsimonious method for calculating the velocity distribution within the channel cross-section as only bathymetric data are required.

In this study, the dimensionless isovel coefficient corresponding to the point with the highest surface velocity is called η_s and is defined as:

$$\eta_s = \frac{V_{s,max}}{U_{mean}} \tag{11}$$

It is worth to note that η_s is the inverse of $\emptyset_s$. The accuracy of this method is affected by the channel bed control, non-uniformity of the cross section, irregular flow directions and presence of singularities. The choice of the cross-section is therefore crucial. This choice must follow the

common rules for gauging using the velocity-area method, i.e. reach of river as uniform as possible, with quasi 1D velocities.

To the knowledge of the authors, this study is the first application of the Isovel model in irregular cross-sections as all other applications of this method has been done on wide regular sections.

For each video records analysed with Fudaa-LSPIV, the value of water level in the "LSPIV cross-section", i.e. H_{LSPIV}, as well as the appropriate bathymetry, were entered to apply the Isovel model. This resulted in the value of η_s. The spatial coordinates of the point corresponding to η_s were also extracted in order to give the position of the "y axis". U_{mean_Isovel} was then calculated as the product of V_{s,max_LSPIV} by the value of $\frac{1}{\eta_s}$. Finally, the slope of the regression between all pairs of (V_{s,max_LSPIV}, U_{mean_Isovel}) was calculated.

2.5.3 Calibrated relation using LSPIV results

For each video records, U_{mean_LSPIV} was calculated by dividing the value of discharge Q by A_{wet} in the "LSPIV cross-section". The value of discharge was obtained through the LSPIV analysis as described in section 2.4. The value of A_{wet} was derived from the H-A_{wet} relation for the value of H_{LSPIV}. Historical pairs of V_{s,max_LSPIV} and U_{mean_LSPIV} were then plotted and the slope of the linear regression forcing to go through the zero intercept was computed. This method is similar to the preferred method used by Fulton et al. (2020) for computing the value of ϕ with the Entropy model. However, in the present case, the slope of the V_{s,max_LSPIV}-U_{mean_LSPIV} gives the value of ϕ_s.

2.5.4 Q-Commander

The Sommer company has developed the Q-Commander software in order to process velocity measured with surface velocity radars (e.g. RG-30, RQ-30). This software gives the distribution of the dimensionless k-factor throughout the cross-section. The k-factor is the ratio between the bulk velocity and the measured local velocity at the surface. It is therefore analogous to the inverse of η of the Isovel model. The documentation of the software (Sommer, 2013) states that the value of the k-factor is usually in the range of 60 to 120% for suitable flow measurement sites, depending on the shape of the profile, the actually measured water level, the position of the radar sensor, and the roughness of the profile. As input, the software requires the profile of the cross-section, the roughness of the river bed and the lateral position of the radar sensor in the cross-section. Subsequently, the cross-section area and the k-factor are automatically calculated for each defined water level value. The equations used in the model are not available, but the model is based on the universal logarithmic law of the wall and considers the influence of the complete cross-section (Sommer, 2013). In this study, the version 2.0.3.5 of the Q-commander software was used. The conditions (i.e. profile of the cross-section, value of the water level) of each video records analysed with Fudaa-LSPIV were used as input, the roughness was set to 100 (gravel bed) and the position that gives the lowest k-factor value was sought in the cross-section. Such a position corresponds to the "y axis" and the lowest value of the k-factor corresponds to ϕ_s. $U_{mean\_Commander}$ was then calculated as the product of V_{s,max_LSPIV} by the lowest value of k-factor. Finally, the slope of the regression between all pairs of (V_{s,max_LSPIV}, $U_{mean\_Commander}$) was calculated.

2.6 Discharge time series calculation

2.6.1 Relation between V_{rad} and V_{s,max_LSPIV}

In this study, the index velocity is V_{rad}, monitored from the downstream side of the bridge. In order to apply the theoretical framework of the index velocity method with the objective of deriving time series of discharge, a relation has to be built between V_{rad} and U_{mean}. At the moment, different methods have been presented to build a linear relation between V_{s,max_LSPIV} and U_{mean} in the "LSPIV cross-section". A complementary relation has to be established between V_{rad} measured from the downstream side of the bridge in the "radars cross-section" and V_{s,max_LSPIV} in the "LSPIV cross-section". For each video records analysed with Fudaa-LSPIV, the value of V_{s,max_LSPIV} was extracted and the synchronized value of V_{rad} was also retrieved. Historical pairs of V_{rad} and V_{s,max_LSPIV} were then plotted and a linear regression was computed.

2.6.2 Discharge algorithm

The procedure was designed to calculate continuously water discharge (Q) from the variables H_{rad} and V_{rad} monitored by the H-V radars at each time step (t). To accomplish this, the methodology can be summarised as follows:

1) The periods with stable bathymetry were identified from the analysis of the H_{rad}-V_{rad} data series and the corresponding H-A_{wet} relations were calculated using the AreaComp version 2.1 software

2) At each time step, $H_{rad}(t)$ in the "radars cross section" was converted into $H_{LSPIV}(t)$ in the "LSPIV cross section" by applying a linear transformation that considers the slope and the distance between the "radars cross-section" and the "LSPIV cross-section" (reduction of 0.2 m in water level)

3) At each time step, $A_{wet}(t)$ in the "LSPIV cross section" was calculated using $H_{LSPIV}(t)$ and the corresponding H-A_{wet} relation

4) At each time step, $V_{rad}(t)$ was transformed into $V_{s,max\_LSPIV}(t)$ using the V_{rad}-V_{s,max_LSPIV} linear relation that enables to shift from the "radars cross section" to the "LSPIV cross section" (see section 2.6.1)

5) At each time step, $U_{mean}(t)$ was calculated using one of the V_{s,max_LSPIV}-U_{mean} linear relations presented in section 2.5. In this study, the relation calibrated with LSPIV results was selected.

6) At each time step, Q(t) was calculated as the product of $U_{mean}(t)$ by $A_{wet}(t)$.

2.6.3 Uncertainty

An analysis of the uncertainty in the procedure of calculation of discharge time series was carried out. Given that Q(t) is calculated as the product of $U_{mean}(t)$ by $A_{wet}(t)$, and considering that the error sources related to $U_{mean}(t)$ and $A_{wet}(t)$ are independent, the squared relative standard uncertainty $u'^2(Q)$ could be expressed following the Guide to the expression of the uncertainty in

535 measurement (ISO/IEC 98-3, 2010) as the sum of the squared standard uncertainties of the error
536 sources:

537 $$u'^2(Q) = u'^2(U_{mean}) + u'^2(A_{wet}) \quad (12)$$

538 Considering that U_{mean} is obtained from two independant linear relations applied consecutively,
539 $u'^2(U_{mean})$ is expressed as follows:

540 $$u'^2(U_{mean}) = u'^2(V_{rad}) + u'^2\left(\left(V_{rad}, V_{s,\max\_LSPIV}\right)_{rating}\right) + u'^2\left(\left(V_{s,\max\_LSPIV}, U_{mean}\right)_{rating}\right) \quad (13)$$

541 Similarly, considering that A_{wet} is obtained from a non-linear relation depending on the
542 bathymetric profile of the "LSPIV cross-section" and the value of H_{LSPIV} which itself is derived
543 from H_{rad} using the slope and the distance between the "radars cross-section" and the "LSPIV
544 cross-section", $u'^2(A_{wet})$ is expressed as follows:

545 $$u'^2(A_{wet}) = u'^2(bathymetry) + u'^2(H_{rad}) + u'^2(slope) \quad (14)$$

The standard uncertainties $u'(V_{rad})$ and $u'(H_{rad})$ are calculated as the standard relative errors of the variables V_{rad} and H_{rad} which are the standard deviations divided by the means. The standard uncertainties $u'\left((V_{rad}, V_{s,\max\_LSPIV})_{rating}\right)$ and $u'\left((V_{s,\max\_LSPIV}, U_{mean})_{rating}\right)$ are the residual standard errors of the linear regressions. The standard uncertainty $u'(slope)$ is calculated as the standard uncertainty of an equiprobable rectangular distribution considering that the slope between the "radars cross-section" and the "LSPIV cross-section" can vary by 0.3% around the value of 2% used in this study. Finally, the standard uncertainty $u'(bathymetry)$ is the most difficult to estimate. An assumption is made that the standard uncertainty in the bathymetric profile of the "LSPIV cross-section" is 10%.

By following this simplified approach, it was possible to calculate a standard uncertainty on Q, $u'(Q)$, which is constant whatever the value of Q. The final uncertainty is expressed at the 95% confidence interval considering a normal distribution and using a coverage factor of 2.

3 Results

3.1 Detection of bathymetric shifts and related periods

Figure 5 shows the time series of V_{rad} and H_{rad} for the entire study period. As explained already in section 2.2, some periods of missing data are due to the presence of a gravel bar that formed temporarily below the H-V radars. This affects the period from July 2019 to May 2021. Figure 5 also displays the time series of water level at La Robine station, the upstream historical station. At each station, water level is expressed in a local coordinate system where the zero level corresponds to the zero in the staff level gauge. It can be seen that at certain periods, the water level at La Robine is higher than the water level at RIPLE, while at other periods it is the opposite. This is due to bathymetric shifts that occured at the RIPLE station during certain floods, whereas bathymetric shifts are very unlikely at La Robine station because the river is set over the bedrock.

Figure 6a shows the scatter plot of V_{rad} versus H_{rad} for the entire study period. Six periods with distinct relations between V_{rad} and H_{rad} were identified manually. The temporal limits of these periods were extracted from the time-stamping of the couples of points (H_{rad}, V_{rad}). It is worth mentioning that, even in the absence of the V_{rad} time series as it is the case for many hydrometric stations, it would have been possible to identifiy the bathymetric changes using an automatic shift detection algorithm such as the method presented recently by Darienzo et al. (2021). However, the method used in this study allows a more accurate time stamping of the bathymetric shifts. The end of period 1 was identified to 01/02/2019 10:00 (UTC), the end of period 2 to 23/10/2019 18:00 (UTC), the end of period 3 to 03/11/2019 04:30 (UTC), the end of period 4 to 21/12/2019 04:50 (UTC), the end of period 5 to 22/01/2021 17:50 (UTC). The six periods are represented in Figure 5 using different colours. The vertical dotted lines in Figure 5 indicate the dates of the topographical surveys carried out at the RIPLE station. There is one campaign per period, with the exception of period 3. The surveyed cross-section profiles associated with each period (except period 3) are shown in Figure 6b. The topographic results confirm that the cross-section profiles are significantly different from each other: the change between period 1 and period 2 is characterized by an increase in bed elevation of the order of 20 cm in the centre-right

of the river channel due to deposition of sediment. The changes between period 2 and period 3 and between period 3 and period 4 remain unknown. As period 3 lasted only 11 days, it was not possible to carry out a bathymetric survey during this short period. In fact, during autumn, significant rainfall events can be frequent on soils that are already very moist, likely to produce repeated morphogenic floods (Esteves et al., 2019). Nevertheless, the change between period 2 and period 4 shows an increase in bed elevation over a large part of the left-hand of the cross-section. The change between period 4 and period 5 is marked by a decrease in bed elevation of the order of 50 cm over the width of the river channel due to erosion processes. The change between period 5 and period 6 is marked by a reorganisation of the shape of the cross-section with a very slight tendency towards sedimentation.

It can be seen that the changes of period occurred during flood events. The change between period 1 and period 2 occurred during the first significant flood of the study (01/02/2019), where the maximum radar velocity reached 3.5 m/s. The change between period 2 and period 3 occurred during a period where data were missing at the RIPLE station due to a power failure. However, the data from La Robine station shows that the flood that produced the bathymetric shift (23/10/2019) is of the same order of magnitude as that of the 01/02/2019. The change between period 3 and period 4 occurred during a major flood (03/11/2019) of the study period with maximum radar velocity of 3.5 m/s. The change between period 4 and period 5 occurred at the end of a significant flood (21/12/2019) with maximum radar velocity of 3 m/s. The change between period 5 and period 6 occurred during a small flood (22/01/2021) where the maximum radar velocity reached 1.4 m/s. Although the transitions between these periods are generally caused by floods, not all significant floods cause a change in bathymetry. For instance, the events of 02/03/2020, 04/06/2020 and 10/05/2021 did not produce significant changes in bathymetry whereas they were characterized by significant radar velocities (maximum of 2.0 m/s, 1.5 m/s and 2.1 m/s respectively). The factors controlling these changes in bathymetry are not well known yet even though they are assumed to be linked to bedload transport, and more specifically to the processes of deposition and remobilisation of gravels. On the other hand, it is likely that some bathymetric changes have been missed. In fact, there is still some dispersion in the H_{rad} - V_{rad} relations for the different separated periods. A more detailed identification, still based on the analysis of the relations between V_{rad} and H_{rad} or based on the application of an automatic shift detection method (Darienzo et al., 2021) would be possible but it would lead to more sub-periods and we would face to the problem of lack of bathymetric data. The proposed breakdown is therefore a compromise between the identification of major bathymetric shifts and the availability of topographic data. It is recognized in this study that there remains a significant degree of uncertainty in the bathymetric profiles within the six separate periods. This is taken into account in the uncertainty analysis.

Figure 6c shows the H-A_{wet} relations for periods 1 to 6 (except period 3). The result exhibits a significant change in the H-A_{wet} relation between period 4 and 5 due to the important digging of the river section during the 21/12/2019 flood event. The other bathymetric changes have a more limited impact on the H-A_{wet} relations. The results presented in this section confirm the effectiveness of the method proposed for detection of bathymetric changes. Regular control of the H_{rad} - V_{rad} scatter plot, coupled with bathymetric survey campaigns, enable to identify major changes in bathymetry and attribute corresponding cross-sectional profiles (i.e. H-A_{wet} relations).

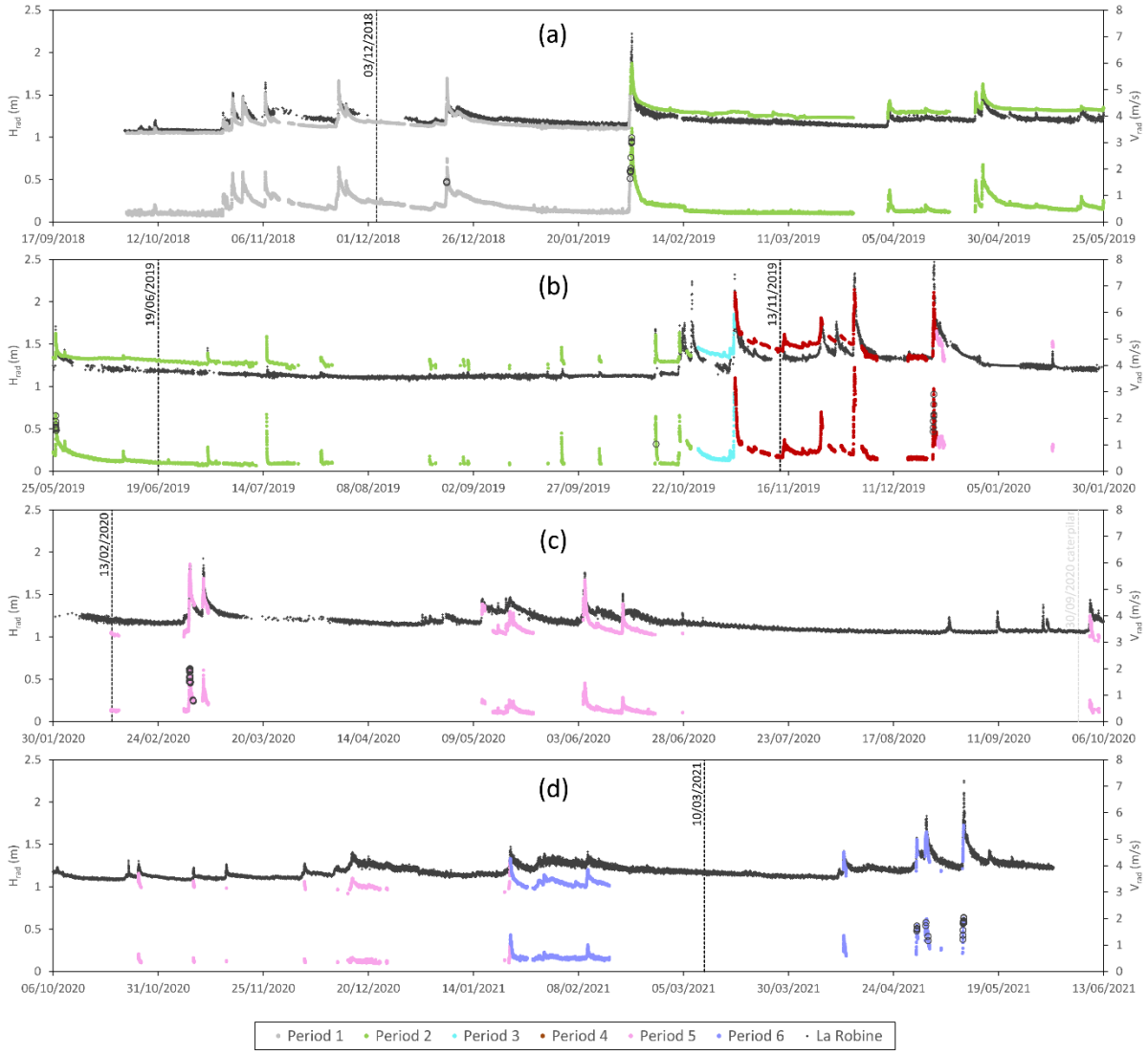

Figure 5 – Time series of H_{rad} (colour data, bottom series, left axis) and V_{rad} (colour data, top series, right axis) at the RIPLE station. Positioning of video sequence recordings on the time series of V_{rad} (black circles). Time series of H_{rad} (black +, left axis) at the Robine station. The vertical dotted lines indicate the dates of the topographical surveys at the RIPLE station.

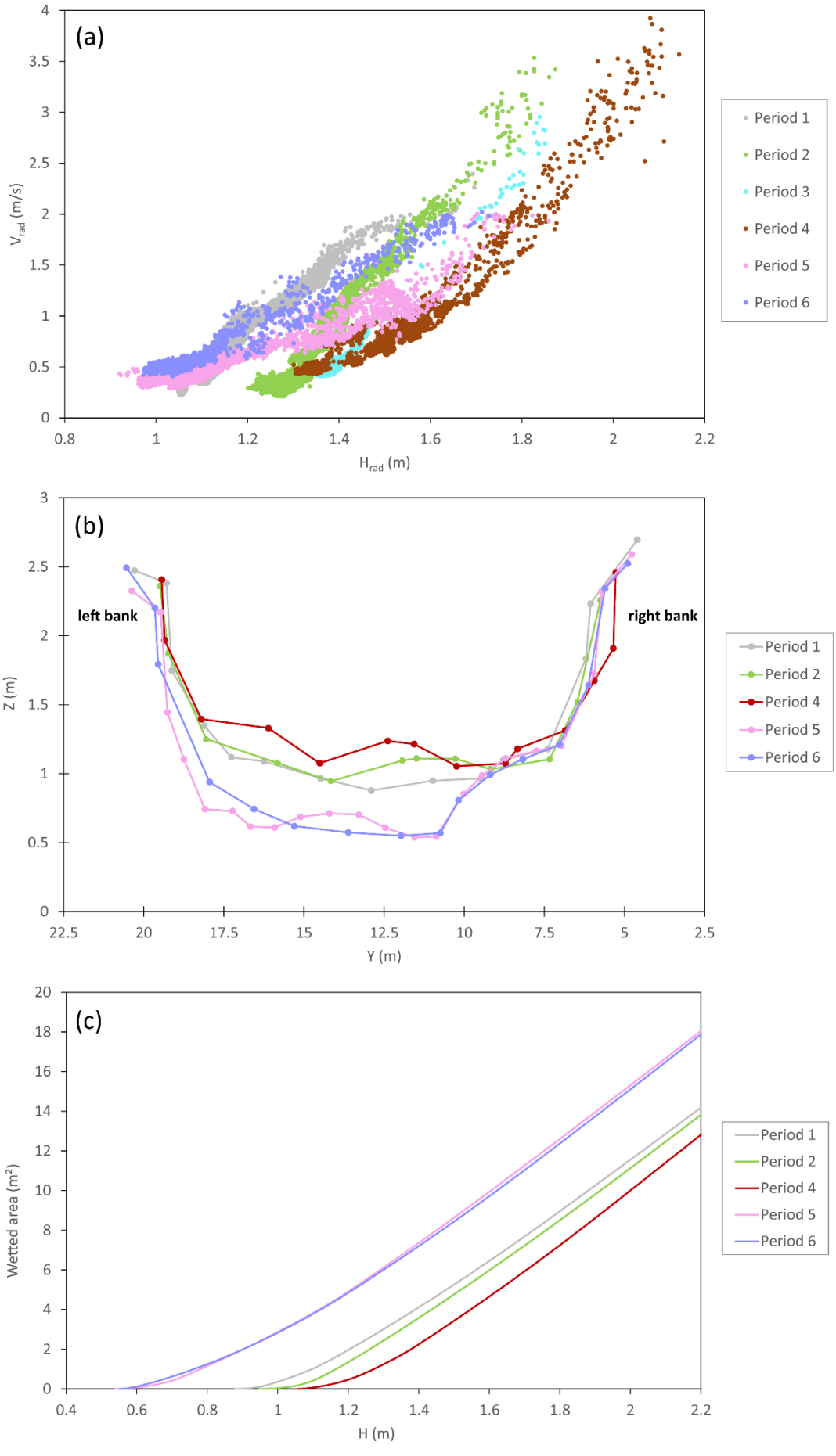
(a)
V_{rad} (m/s)
H_{rad} (m)
Period 1
Period 2
Period 3
Period 4
Period 5
Period 6
(b)
left bank
right bank
Z (m)
Y (m)
Period 1
Period 2
Period 4
Period 5
Period 6
(c)
Wetted area (m²)
H (m)
Period 1
Period 2
Period 4
Period 5
Period 6

Figure 6 – (a) Relation between V_{rad} and H_{rad} at RIPLE distinguished by bathymetric periods. (b) cross-sectional profiles at the "LSPIV cross-section" for each bathymetric period (except period 3). (c) Relations between H (in local coordinate system of RIPLE) and wetted area of the cross-sectional profiles at the "LSPIV cross-section" for each bathymetric period (except period 3).

3.2 LSPIV results

The results of LSPIV analysis are summarized in Table 2. The maximum discharge of 30.76 m^3/s was computed during period 5 for the video taken the 02/03/2020 at 12:43 (UTC) with a value of V_{s,max_LSPIV} of 4.37 m/s and a value of U_{mean_LSPIV} of 2.86 m/s. The lowest discharge of 0.81 m^3/s was computed during period 2 for the video taken the 15/10/2019 at 12:21 (UTC) with a value of V_{s,max_LSPIV} of 1.02 m/s and a value of U_{mean_LSPIV} of 0.71 m/s. Table 2 also gives the values of V_{rad} and H_{LSPIV} at the time steps corresponding to the video recordings. H_{LSPIV} is derived from H_{rad} according to the method described in the section 2.1.

Table 2 – Results of LSPIV analyses carried out on video sequences recorded at the RIPLE station (Q: flow discharge, A_{wet}: wetted area, U_{mean_LSPIV}: mean cross-sectional velocity, V_{s,max_LSPIV}: maximum surface velocity, y axis: lateral position of $V_{s,max}$, $\emptyset_S$: ratio between U_{mean} and $V_{s,max}$). Extraction of radar data (H_{LSPIV} and V_{rad}) at time steps corresponding to the video recordings. Results of the Isovel model for the conditions corresponding to the LSPIV analyses (η_s: highest value of the dimensionless isovel coefficient). Q-Commander software results for the conditions corresponding to the LSPIV analyses (k-$factor_{min}$: lowest value of the dimensionless k-factor in the cross-section)

Date Video Sequence	Period	LSPIV								Isovel		Q-Commander	
		H_{LSPIV}	V_{rad}	A_{wet}	Q	U_{mean_LSPIV}	V_{s,max_LSPIV}	y axis	Φ_s	y axis	$1/\eta_s$	y axis	k-factor$_{min}$
		(m)	(m/s)	(m^2)	(m^3/s)	(m/s)	(m/s)	(m)	(-)	(m)	(-)	(m)	(-)
19/12/2018 15:16	1	1.156	1.48	1.531	1.56	1.02	1.33	11.43	0.77	12.68	0.54	12.90	0.55
19/12/2018 15:46	1	1.180	1.53	1.768	1.86	1.05	1.49	15.31	0.71	12.68	0.55	12.90	0.56
01/02/2019 07:17	1	1.208	1.64	2.055	2.33	1.14	1.65	10.66	0.69	12.66	0.55	12.90	0.57
01/02/2019 07:47	1	1.289	1.92	2.903	4.66	1.61	2.10	11.91	0.77	12.64	0.57	12.90	0.61
01/02/2019 09:17	1	1.307	1.88	3.097	5.67	1.83	2.35	12.10	0.78	12.62	0.57	12.90	0.62
01/02/2019 09:46	1	1.345	1.89	3.511	6.70	1.91	2.48	14.53	0.77	12.62	0.58	12.90	0.63
01/02/2019 10:18	2	1.331	1.93	2.809	4.86	1.73	2.49	14.54	0.69	14.04	0.60	14.15	0.59
01/02/2019 10:48	2	1.363	1.92	3.182	5.67	1.78	2.61	14.54	0.68	13.90	0.61	14.15	0.60
01/02/2019 11:18	2	1.429	2.02	3.953	7.45	1.89	2.72	14.34	0.69	13.82	0.61	14.15	0.63
01/02/2019 11:48	2	1.503	2.44	4.839	10.23	2.11	3.01	13.86	0.70	13.76	0.62	14.15	0.67
01/02/2019 14:47	2	1.537	3.01	5.254	15.77	3.00	3.91	14.34	0.77	13.72	0.62	14.15	0.68
01/02/2019 15:17	2	1.520	3.02	5.045	15.20	3.01	4.06	14.25	0.74	13.74	0.62	14.15	0.67
01/02/2019 15:46	2	1.505	2.99	4.864	14.73	3.03	4.07	14.54	0.74	13.76	0.62	14.15	0.67
01/02/2019 16:17	2	1.560	3.18	5.537	16.99	3.07	4.24	14.44	0.72	13.70	0.62	14.15	0.68
01/02/2019 16:47	2	1.586	3.05	5.859	18.08	3.09	4.03	14.25	0.77	13.66	0.62	14.15	0.57
25/05/2019 14:18	2	1.303	1.63	2.495	2.49	1.00	1.39	13.77	0.72	14.04	0.60	14.15	0.58
25/05/2019 14:48	2	1.392	2.10	3.519	4.83	1.37	2.00	14.25	0.69	13.86	0.61	14.15	0.62
25/05/2019 15:18	2	1.350	1.88	3.032	5.48	1.81	2.62	14.15	0.69	14.04	0.60	14.15	0.60
25/05/2019 16:18	2	1.328	1.67	2.780	5.15	1.85	2.77	14.05	0.67	14.04	0.60	14.15	0.59
25/05/2019 16:48	2	1.306	1.64	2.530	4.09	1.62	2.13	13.96	0.76	14.04	0.60	14.15	0.58
25/05/2019 17:18	2	1.291	1.59	2.360	3.21	1.36	1.95	14.15	0.70	14.04	0.59	14.15	0.57
25/05/2019 17:48	2	1.283	1.54	2.271	3.13	1.38	1.89	14.15	0.73	14.06	0.59	14.15	0.57
15/10/2019 12:21	2	1.177	1.02	1.132	0.81	0.71	1.02	14.54	0.70	14.08	0.58	9.18	0.49
20/12/2019 10:17	4	1.472	1.50	3.113	5.31	1.70	2.73	14.18	0.62	10.00	0.63	10.23	0.61
20/12/2019 10:47	4	1.500	1.65	3.449	6.40	1.86	2.77	13.51	0.67	10.02	0.64	10.23	0.62
20/12/2019 11:17	4	1.537	1.79	3.900	7.91	2.03	3.18	13.80	0.64	10.06	0.63	10.23	0.64
20/12/2019 13:18	4	1.868	2.90	8.204	29.04	3.54	5.51	14.37	0.64	10.48	0.63	10.23	0.70
20/12/2019 13:48	4	1.690	2.52	5.826	19.75	3.39	5.11	14.54	0.66	10.22	0.63	10.23	0.68
20/12/2019 14:17	4	1.674	2.14	5.621	15.91	2.83	4.38	13.32	0.65	10.20	0.63	10.23	0.67
20/12/2019 14:47	4	1.641	2.09	5.197	13.46	2.59	3.84	13.32	0.67	10.16	0.63	10.23	0.67
02/03/2020 09:43	5	1.415	1.52	7.577	16.65	2.20	3.15	12.78	0.70	12.59	0.63	11.54	0.66
02/03/2020 10:13	5	1.474	1.68	8.332	20.59	2.47	3.37	12.14	0.73	12.67	0.63	11.54	0.67
02/03/2020 10:43	5	1.516	1.97	8.876	23.01	2.59	3.69	13.15	0.70	12.73	0.63	11.54	0.68
02/03/2020 11:13	5	1.554	1.95	9.371	25.90	2.76	3.79	13.42	0.73	12.77	0.63	11.54	0.68
02/03/2020 11:43	5	1.539	1.96	9.175	25.15	2.74	3.61	13.15	0.76	12.75	0.63	11.54	0.68
02/03/2020 12:13	5	1.542	1.87	9.214	26.21	2.84	3.92	13.06	0.73	12.75	0.63	11.54	0.68
02/03/2020 12:43	5	1.659	1.95	10.754	30.76	2.86	4.37	13.51	0.65	12.87	0.63	11.54	0.69
02/03/2020 13:43	5	1.582	1.88	9.735	25.95	2.67	4.12	13.88	0.65	12.81	0.63	11.54	0.68
02/03/2020 14:13	5	1.543	2.00	9.224	25.76	2.79	4.18	13.97	0.67	12.75	0.63	11.54	0.68
02/03/2020 14:43	5	1.538	1.73	9.159	25.52	2.79	4.12	13.61	0.68	12.75	0.63	11.54	0.68
02/03/2020 15:13	5	1.497	1.66	8.627	22.50	2.61	3.68	14.84	0.71	12.71	0.63	11.54	0.67
02/03/2020 15:43	5	1.473	1.52	8.318	20.16	2.42	3.52	14.79	0.69	12.67	0.63	11.54	0.67
02/03/2020 16:13	5	1.479	1.46	8.395	21.46	2.56	3.50	14.79	0.73	12.67	0.63	11.54	0.67
02/03/2020 16:43	5	1.457	1.49	8.112	20.58	2.54	3.52	14.70	0.72	12.65	0.63	11.54	0.67
03/03/2020 06:43	5	1.235	0.82	5.348	6.35	1.19	1.80	15.33	0.66	12.35	0.63	11.54	0.63
03/03/2020 07:43	5	1.227	0.80	5.251	6.12	1.17	1.76	14.97	0.66	12.35	0.63	11.54	0.63
03/03/2020 09:43	5	1.213	0.77	5.084	5.59	1.10	1.69	15.06	0.65	12.33	0.63	11.54	0.63
29/04/2021 12:12	6	1.316	1.53	6.323	12.40	1.96	2.83	13.33	0.69	13.07	0.60	12.00	0.66
29/04/2021 12:42	6	1.340	1.59	6.613	11.71	1.77	2.80	14.00	0.63	13.07	0.60	12.00	0.66
29/04/2021 13:16	6	1.340	1.72	6.613	11.76	1.78	2.74	13.62	0.65	13.07	0.60	12.00	0.66
29/04/2021 13:42	6	1.308	1.63	6.226	10.41	1.67	2.70	14.00	0.62	13.07	0.60	12.00	0.66
01/05/2021 15:46	6	1.396	1.73	7.298	15.88	2.18	3.15	13.33	0.69	13.07	0.60	12.00	0.67
01/05/2021 16:16	6	1.406	1.85	7.423	16.57	2.23	3.22	11.88	0.69	13.07	0.60	12.00	0.67
02/05/2021 04:42	6	1.206	1.32	5.022	7.15	1.42	2.24	14.57	0.63	13.05	0.59	12.00	0.64
02/05/2021 05:12	6	1.188	1.33	4.818	6.59	1.37	2.28	14.57	0.60	13.05	0.59	12.04	0.64
02/05/2021 05:42	6	1.162	1.16	4.527	6.35	1.40	2.31	14.57	0.61	13.05	0.59	12.15	0.65
10/05/2021 11:42	6	1.150	1.21	4.396	6.10	1.39	2.27	14.57	0.61	13.05	0.59	12.20	0.65
10/05/2021 12:12	6	1.212	1.37	5.092	7.35	1.44	2.49	14.38	0.58	13.05	0.59	12.00	0.64
10/05/2021 12:42	6	1.258	1.56	5.631	8.99	1.60	3.00	14.09	0.53	13.05	0.59	12.00	0.65
10/05/2021 13:12	6	1.312	1.81	6.275	11.02	1.76	2.99	13.62	0.59	13.07	0.60	12.00	0.66
10/05/2021 13:42	6	1.358	1.84	6.832	13.07	1.91	3.01	14.00	0.63	13.07	0.60	12.00	0.66
10/05/2021 14:16	6	1.440	1.87	7.847	17.60	2.24	3.31	12.94	0.68	13.07	0.61	12.00	0.67
10/05/2021 14:46	6	1.440	1.88	7.847	17.50	2.23	3.41	13.23	0.65	13.07	0.61	12.00	0.67
10/05/2021 15:16	6	1.486	1.91	8.428	19.31	2.29	3.37	12.65	0.68	13.07	0.61	12.00	0.68
10/05/2021 15:46	6	1.514	2.02	8.785	23.78	2.71	3.86	14.29	0.70	13.07	0.61	12.00	0.68
10/05/2021 16:16	6	1.510	2.04	8.734	24.23	2.78	3.89	12.84	0.71	13.07	0.61	12.00	0.68
10/05/2021 16:46	6	1.554	1.92	9.302	26.22	2.82	4.05	12.55	0.70	13.07	0.61	12.00	0.68
10/05/2021 17:16	6	1.588	1.90	9.748	26.72	2.74	4.02	12.94	0.68	13.07	0.61	12.00	0.68
10/05/2021 17:46	6	1.574	1.85	9.564	27.24	2.85	4.10	12.55	0.69	13.07	0.61	12.00	0.68

3.3 The V_{s,max_LSPIV}-U_{mean} relation in the "LSPIV section"

3.3.1 Calibrated relation using LSPIV results

Based on data presented in Table 2, the mean cross-section velocity calculated with LSPIV results (U_{mean_LSPIV}) was plotted against the maximum surface velocity (V_{s,max_LSPIV}) in Figure 7 for each bathymetric period (except period 3). Linear regressions forcing to go through the zero intercept were calculated between the two variables. The statistic results of the linear regressions are presented in Table 3. Significant coefficients of determination (between 0.798 and 0.947) are obtained for all periods. The values of the slope of these different regressions are then compared. They range between 0.652 (period 4) and 0.755 (period 1). The interval of confidence of these slopes are also calculated. The assumption to be tested is the resistance of the V_{s,max_LSPIV}-U_{mean_LSPIV} relation to bathymetric shifts. From a strictly statistical point of view, this assumption is not validated here since the 95% confidence intervals of the different regressions do not completely overlap. However, taking into account the relatively small number of points for certain periods (e.g. 6 and 7 observations for periods 1 and 4 respectively) and the uncertainties associated with the LSPIV method for the estimation of V_{s,max_LSPIV} and U_{mean_LSPIV} (uncertainties in the image analysis method and in the bathymetry for the calculation of U_{mean_LSPIV}), it seems reasonable to conclude that the differences between the periods are sufficiently small so that the periods can be combined together to calculate an overall regression. Figure 7 shows the linear relation between V_{s,max_LSPIV} and U_{mean_LSPIV} for all periods combined together. Tha data of Figure 7 are also reproduced in Figure 8 for intercomparison with the results of the Isovel model and the Q-Commander model. The slope of the global regression is 0.686 and its 95% interval confidence is ± 0.011 (Table 3). In conclusion, there seems to be a proportionality between V_{s,max_LSPIV} and U_{mean_LSPIV}. Moreover this linear relation appears to be independent of bathymetric shifts with a single stable and robust slope, which would represent an intrinsic property of the cross-section.

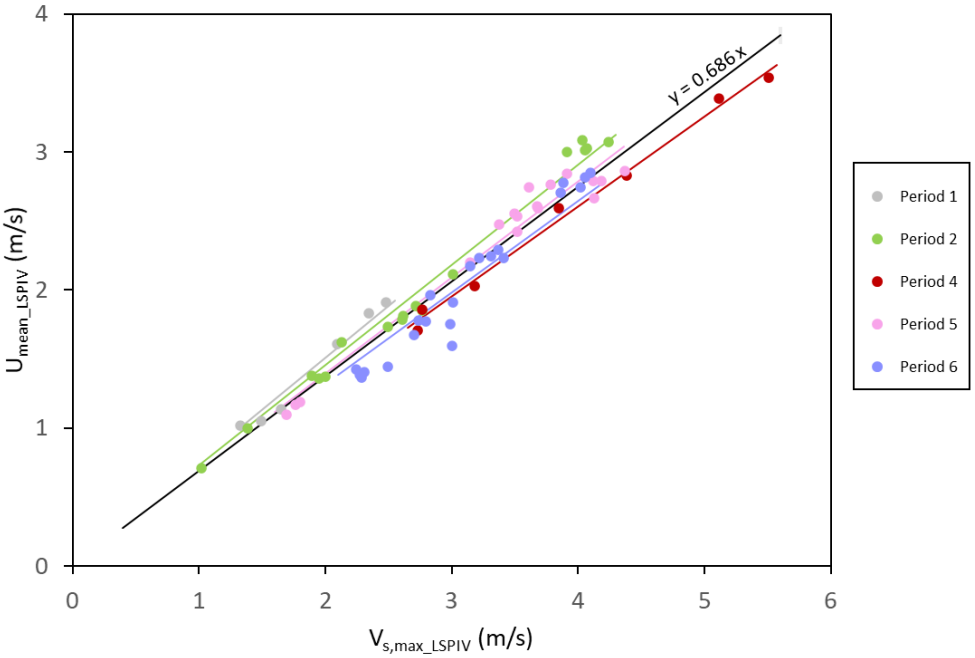

682 **Figure 7 – Relation between U_{mean_LSPIV} and V_{s,max_LSPIV} for each bathymetric period (except period 3). A linear regression forcing to go**
683 **through the zero intercept is fitted for each bathymetric period and for all periods combined together (black line).**

684
685
686
687
688
689
690
691
692
693
694
695
696
697
698
699
700
701
702
703
704
705
706 **Table 3 – Statistic results of the linear regressions (forcing to go through the zero intercept) between U_{mean_LSPIV} and V_{s,max_LSPIV} using**
707 **LSPIV results for each bathymetric period (except period 3) and for all periods combined together.**

	Period 1	Period 2	Period 4	Period 5	Period 6	All period
Coefficient of determination R^2	0.798	0.936	0.833	0.935	0.947	0.981
Standard error	0.068	0.094	0.063	0.121	0.149	0.150
Observations	6	17	7	17	22	69
Slope	0.755	0.726	0.652	0.698	0.661	0.686
Lower limit for 95% confidence level	0.719	0.710	0.637	0.680	0.639	0.675
Upper limit for 95% confidence level	0.792	0.743	0.666	0.715	0.682	0.698

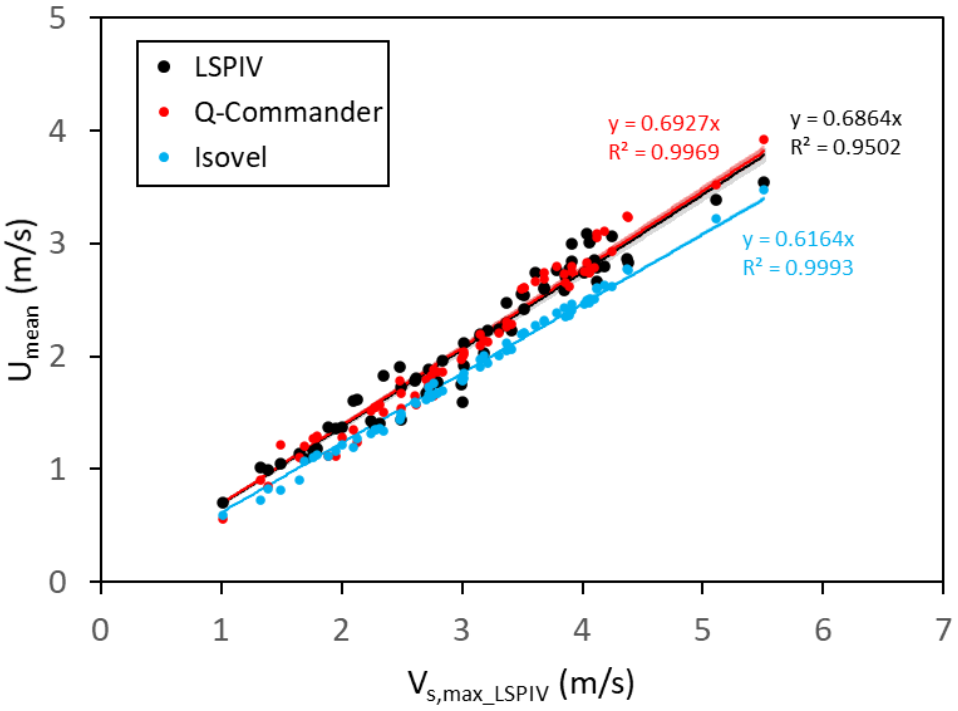

Figure 8 – Relation between U_{mean} and V_{s,max_LSPIV} for all the conditions reported in Table 2. U_{mean} is obtained by three methods: LSPIV results, Isovel model and Q-Commander model. A linear regression forcing to go through the zero intercept is fitted for each approach. The 95% confidence interval associated with the linear regression for the LSPIV case is shown in grey.

3.3.2 Isovel model

As seen in Table 2, the value of $\frac{1}{\eta_s}$ ranges between 0.54 and 0.64, with an average of 0.61 and a standard deviation of 0.02. Figure 8 represents U_{mean} calculated by the Isovel model (U_{mean_Isovel}) versus V_{s,max_LSPIV} derived from the LSPIV analysis for the 69 conditions of Table 2. The linear regression forcing to go through the zero intercept gives a slope of 0.616. This value is 10% lower than the slope of the calibrated regression using LSPIV but it can be considered as an acceptable result given that the Isovel method as applied in this study only requires bathymetric and water level information as input.

3.3.3 Q-Commander

As seen in Table 2, the value of the k-factor$_{min}$ ranges between 0.49 and 0.70, with an average of 0.64 and a standard deviation of 0.04. Figure 8 represents U_{mean} calculated by the Q-Commander

724 software ($U_{mean\_Commander}$) versus V_{s,max_LSPIV} for the 69 conditions of Table 2. The linear
725 regression forcing to go through the zero intercept gives a slope of 0.69. This value is of the
726 same order of magnitude as the slope of the calibrated relation using LSPIV results. Q-
727 Commander is therefore the tool that produces the best prediction of the V_{s,max_LSPIV}-U_{mean_LSPIV}
728 relation. Q-Commander is potentially an effective tool to be used for future applications.
729 However, given that Q-Commander is a commercial software whose code is covered by a patent,
730 the equations used in the model are not available. It is therefore important to continue working
731 with methods such as the Isovel model or the Entropy model to understand which factors control
732 the linear relation between $V_{s,max}$ and U_{mean}.

733 3.4 Position of the "y axis"

734 Figure 9 exhibits the position of the "y axis" for all the conditions reported in Table 2 based on
735 LSPIV results. The results are grouped by bathymetric period. The cross-sectional profiles at the
736 "LSPIV section" for each bathymetric period are also displayed. Figure 10a shows the box plots
737 of the "y axis" position for each bathymetric period. The mean value of the position of the "y
738 axis" is 12.7 m (standard deviation of 1.8 m), 14.2 m (standard deviation of 0.2 m), 13.9 m
739 (standard deviation of 0.5 m), 14.0 m (standard deviation of 0.9 m), 13.6 m (standard deviation
740 of 0.8 m) for period 1, 2, 4, 5, and 6 respectively. The position of the "y axis" is relatively
741 constant for periods 2 to 6. The maximum relative difference is 2% compared to the average of
742 the 4 periods, which is 13.9 m. The maximum relative difference is also 2% compared to the
743 river at bank-full discharge, which is approximately 13.8 m. The standard deviation values for
744 periods 2 to 6 are all lower than 1 m. For period 1, the results are more scattered. The average
745 position of the "y axis" for period 1 is 1.2 m lower than the average value of periods 2 to 6. This
746 represents a relative difference of 8.6% compared to the average of periods 2 to 6. Period 1
747 includes 3 of the 5 smallest discharge values in Table 2. Such discharges are associated with low
748 water depths, as seen in Figure 9, and "y axis" positions that are located both furthest to the left
749 and right sides of the dataset. This may be due to the poorer quality of the LSPIV analyses for
750 low flow conditions and also to the fact that period 1 includes only six observations. Apart from
751 these few outliers, the position of the "y axis" can be considered stable in spite of the
752 bathymetric changes.

753 In Figure 10b, the data from the different bathymetric periods are grouped together and box plots
754 of the position of the "y axis" are represented for the three methods used in this study (LSPIV,
755 Isovel, and Q-Commander). Based on LSPIV results, the mean value of the "y axis" position is
756 13.8 m and the median is 14 m. For the Isovel model, the mean value of the "y axis" position is
757 12.8 m, the median is 13 m and the standard deviation is 1 m. For Q-Commander, the mean
758 value of the "y axis" position is 12.3 m, the median is 12 m and the standard deviation is 1.3 m.
759 The Isovel model and the Q-Commander software predict the average position of the "y axis"
760 respectively 1 m and 1.5 m closer to the right bank than the LSPIV method. This represents a
761 lateral shift of 7% and 11% respectively, considering the width of the river at bank-full
762 discharge, compared to the mean value of the LSPIV method. The standard deviation of the "y
763 axis" for these two methods is of the same order of magnitude as for the LSPIV results (0.9%).

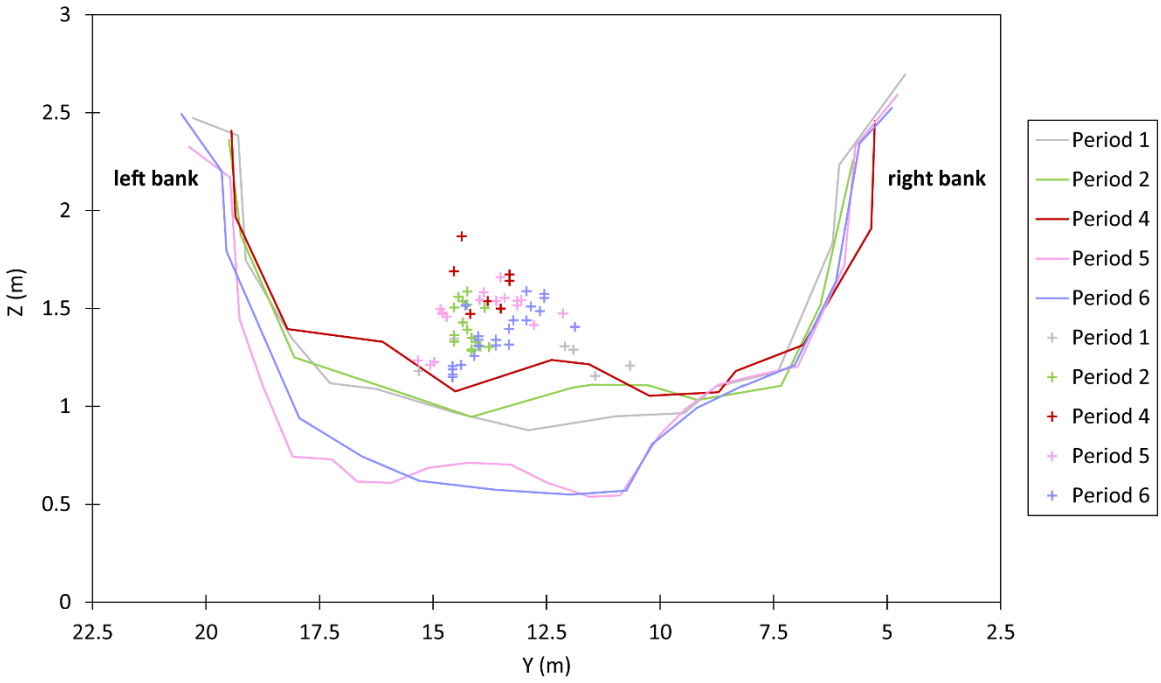

764

765 **Figure 9 – Cross-sectional profiles at the "LSPIV section" for each bathymetric period (except period 3) and location of the "y axis",**
766 **which corresponds to the point of maximum surface velocity, for all the conditions reported in Table 2 based on LSPIV results.**

767 In conclusion, the results show that the position of the "y axis" is relatively stable despite strong
768 bathymetric changes. On the other hand, the theoretical methods (Isovel and Q-Commander)
769 predict satisfactorily the mean position of the "y axis" compared to the LSPIV results even
770 though more data is still needed to verify these assertions.

771

772

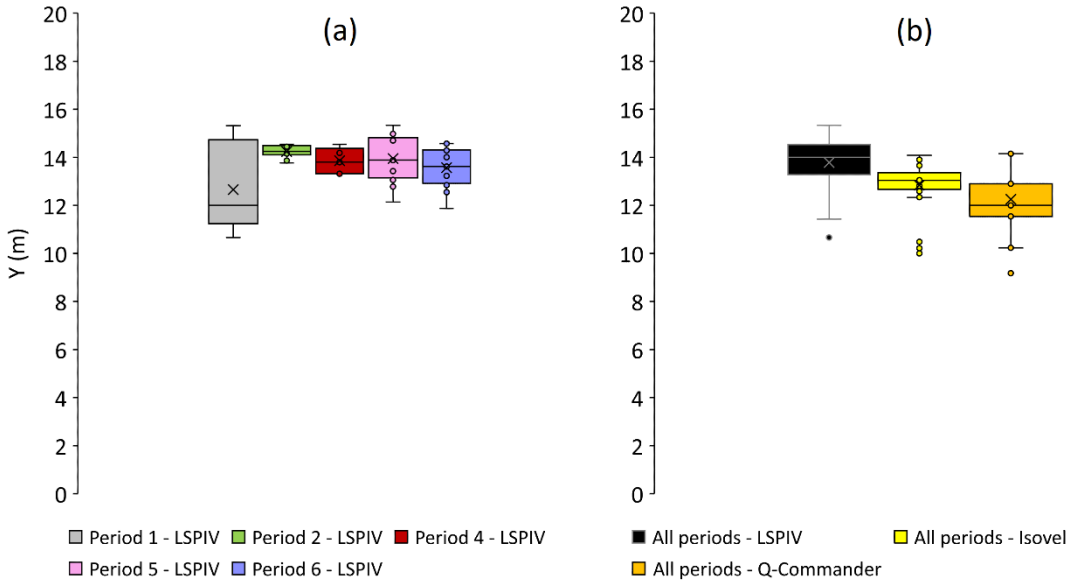

773

774 **Figure 10 – (a) Box and whisker plots of "y axis" positions represented by bathymetric periods (except period 3) based on LSPIV results**
775 **reported in Table 2. (b) Box and whisker plots of "y axis" positions for all periods combined together (except period 3) based on LSPIV,**
776 **Isovel model and Q-Commander results reported in Table 2**

777

778 ## 3.5 Calculation of discharge time series

779 ### 3.5.1 Calibrated relation between V_{rad} and V_{s,max_LSPIV}

780 As described in section 2.6.2, a relation needs to be established between V_{rad} measured in the
781 "radars section" and V_{s,max_LSPIV} obtained in the "LSPIV section" before V_{s,max_LSPIV} can be
782 transformed into U_{mean}. Figure 11 presents the scatter plot of V_{s,max_LSPIV} versus V_{rad}. Two groups
783 of periods were distinguished: periods 1 to 2 on one hand, periods 4 to 6 on the other hand.
784 Figure 11 also shows the linear regression fitted for each group of periods as well as their 95%
785 confidence intervals. The coefficient of determination is high for each of the linear regressions,
786 with R^2=0.9015 for periods 1 to 2 and R^2=0.8111 for periods 4 to 6. The reasons for this change
787 in the linear relation are not entirely clear. It seems to be linked to a shift in the morphological
788 behaviour between the "radars section" and the "LSPIV section". There may have been a
789 localised and temporary scouring of the riverbed in the vicinity of the bridge where the radars are
790 installed caused by the hydraulic jump in the upper part of the bridge.

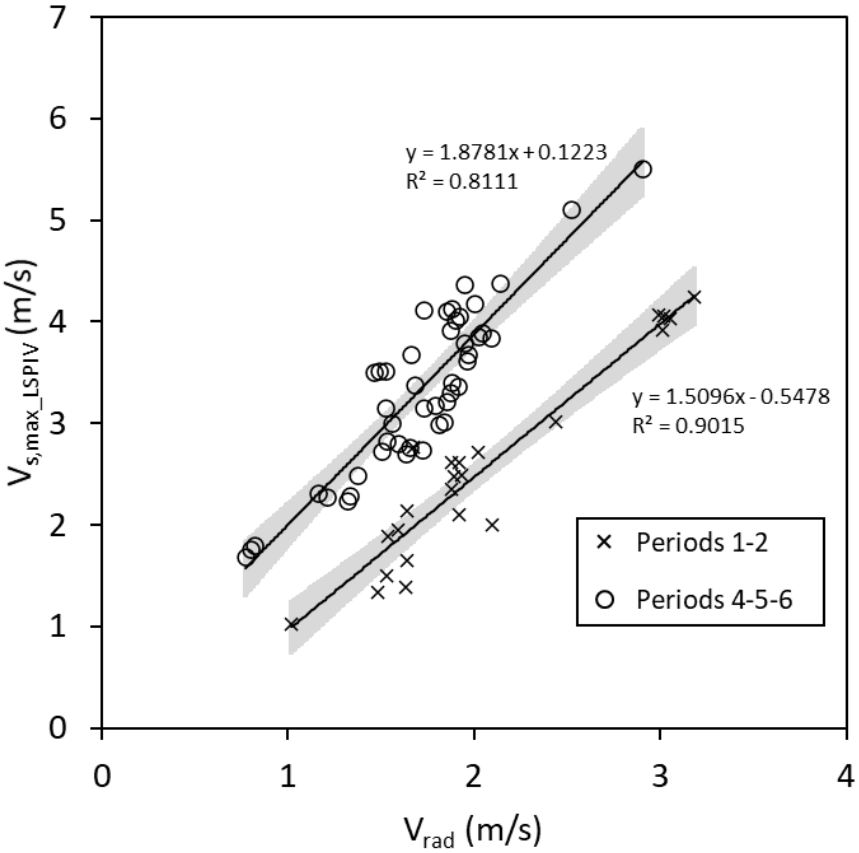

Figure 11 – Relations between V_{s,max_LSPIV} in the "LSPIV section" and V_{rad} in the "radars section" based on the results reported in Table 2 for two different groups of periods. A linear regression is fitted for each group of periods. The 95% confidence intervals associated with the linear regressions are shown in grey.

4 Discussion

4.1 Evaluation of the method

4.1.1 Comparison with the historical station at La Robine

The discharge algorithm was applied to the data at RIPLE for the period from October 2018 to May 2021, except period 3 (from 23/10/2019 to 03/11/2019) due to the absence of bathymetric data. The discharge time series at RIPLE, expressed as specific discharge of the drainage area (in $m^3/s/km^2$), are shown in Appendix 1. The discharge time series at La Robine are also represented in Appendix 1 as they provide the only comparative data for assessing the method presented in this study. The Galabre catchment at la Robine station drains a surface of 20 km^2 compared with a surface of 34 km^2 at the RIPLE station. This corresponds to a 41% increase in the drained area of the catchment from La Robine station to RIPLE station. Therefore, a very good match between the data of the 2 stations cannot be expected, even in the case of perfectly accurate data, because of the hydrological processes involved (spatial distribution of rainfall, heterogeneity of soils properties, land cover, and infiltration, role of the alluvial water table) and the phenomenon

of flood wave propagation. In general, the data seem to match up well. Table 4 presents the statistics of the comparison between the specific discharge at the two stations for all the time steps of the study period, except when data is missing at one of the stations. Both stations have the same sampling period (e.g. 10 min). Results are obtained by comparing data of the two stations at the same time step. The time lag associated with the transfer of water from upstream to downstream is neglected in this comparison. The time lag between peak discharge at the two stations during floods is short, generally on the order of 10 to 20 min and possibly up to 30-40 min for small floods in spring and summer. Outside the floods, there is no need to consider a time lag as the regime is considered permanent. Anyway, the data were compared with and without a time lag, but there was no gain in the results when a time lag was considered.

Table 4 – Statistic results of the comparison between the specific discharge at La Robine and RIPLE stations for all the data of the study.

	all data	$V_{rad} > 0.7$ m/s	$V_{rad} < 0.7$ m/s
Nash-Sutcliffe efficiency (NSE)	0.877	0.863	0.580
Log Nash-Sutcliffe efficiency (logNSE)	0.248	0.738	-0.084
Percent Bias (PBIAS)	4.5	2.9	8.7

Three statistical results are given in Table 4: the Nash-Sutcliffe efficiency (NSE), the log Nash-Sutcliffe efficiency (logNSE), and the percent bias (PBIAS). The NSE provides information about the deviation of the specific discharge at RIPLE compared to the specific discharge at La Robine. Applying the NSE to the logarithm of discharges (logNSE) enables to assess the behaviour of the prediction at low flow discharges. PBIAS provides information on the existence of a simulation bias (negative or positive), expressed as a %, between the two variables.

The data are considered as a whole (all data) and then divided into two groups according to the value of the fixed velocity radar: $V_{rad} > 0.7$ m/s and $V_{rad} < 0.7$ m/s. The values of NSE are good (i.e. in the range 0.86-0.88) for "all data" and the " $V_{rad} > 0.7$ m/s" group and less good (0.58) for the " $V_{rad} < 0.7$ m/s" group. The logNSE value is reasonably good (0.738) for the " $V_{rad} > 0.7$ m/s" group, but much worse (0.248) for "all data", and poor (-0.084) for the " $V_{rad} < 0.7$ m/s" group. The PBIAS value is the lower (2.9%) for the " $V_{rad} > 0.7$ m/s" group, intermediate (4.5%) for “all data”, and the higher (8.7%) for the " $V_{rad} < 0.7$ m/s" group. These results show that the comparison between specific discharges at the two stations is generally acceptable for “all data”. This comparison is better when V_{rad} is above 0.7 m/s. In contrast, below this velocity, specific discharges at RIPLE calculated using the approach presented in this study are significantly different from specific discharges at La Robine station calculated using the stage-discharge rating curve, and have an overall tendency to underestimate.

The literature frequently states that surface velocity radars do not perform well in the low-velocity range (Welber et al., 2016; Fulton et al., 2020; Rahman Khan et al., 2021; Son et al., 2023), even though manufacturers claim that instrument sensitivity and resolution are good even at low velocities. In fact, the environmental conditions encountered for low velocities make measurements less reliable. Sources of error in this velocity range (typically below 0.7 m/s) include (i) wind, which has a more detrimental effect than at higher velocities; (ii) the higher distance between the sensor and the free surface compared to high flow conditions, which

increases the sampled area and thus the variability of the measurement; and (iii) the diversity of hydraulic micro-controls, which can occur at low water levels due to the exposition of boulders.

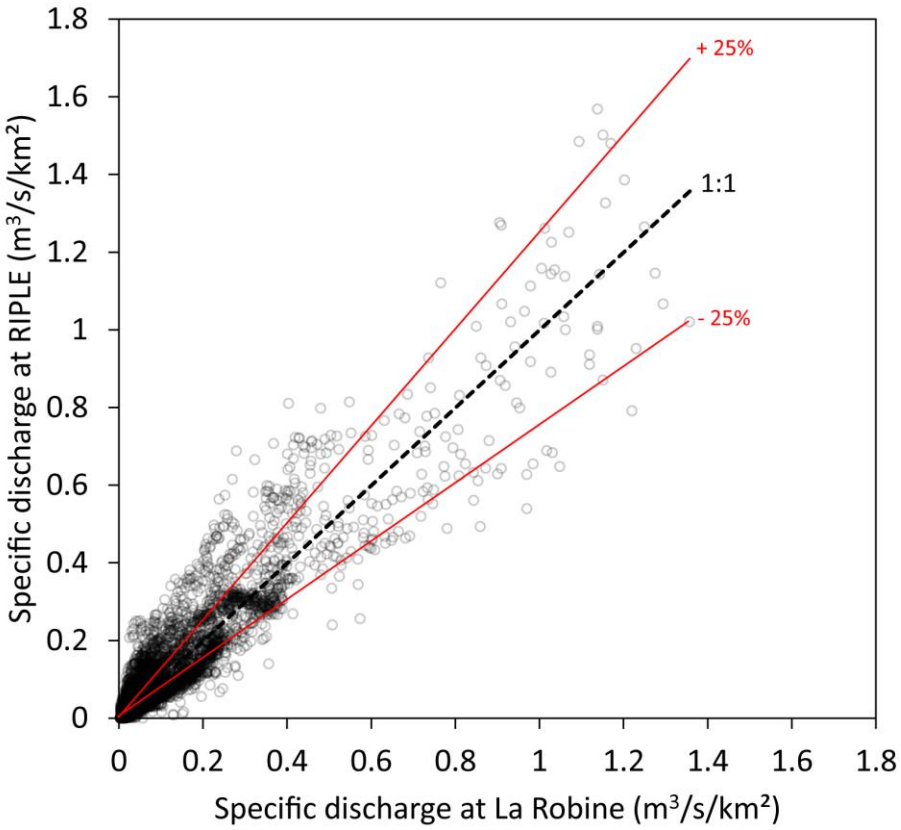

Figure 12 – Specific discharge at the RIPLE station versus specific discharge at La Robine station for all the study period.

Figure 12 shows the same data as in Appendix 1 but in the form of a scatter plot of specific discharges at the two stations. First of all, the regression between the two variables was calculated. It gives a slope equal to unity, an intercept of almost zero, and a coefficient of determination of 0.88. This confirms the good general agreement between the two variables and the general absence of bias. However, the two variables are better correlated for higher values than for lower values. This finding is supported by the results of Table 5 which presents the percentages of values of specific discharge at RIPLE that belong to the ranges ± 25%, ± 50% and ± 100% of the corresponding values at La Robine. Similarly, the lines at ± 25% of the 1:1 line are shown in Figure 12. In Table 5, the data are considered as a whole (all data) and then three subsets are considered according to the value of the fixed velocity radar: $V_{rad} > 0.7$ m/s, $V_{rad} > 1$ m/s, and $V_{rad} > 1.5$ m/s. When "all data" are considered, only 15.7% of the specific discharges calculated at RIPLE belong to the range ± 25% of the corresponding specific discharges at La Robine. On the other hand, when considering the subsets for which the value of V_{rad} is greater than 0.7, 1 and 1.5 m/s, respectively 30.6, 38.4 and 45.6% of the specific discharges calculated at RIPLE fall within the range ± 25% of the corresponding specific discharges at La Robine. These percentages increase significantly when the intervals at ± 50% and ± 100% of corresponding specific flows at La Robine are considered. This corroborates the fact that the results are worse at

low radar velocities (i.e. < 0.7 m/s) and better at higher radar velocities. This velocimetric method is therefore rather reserved to medium to high flow conditions.

Table 5 – Percentages of values of specific discharge at RIPLE within ± 25%, ± 50% and ± 100% of values of specific discharge at La Robine.

	all data	V_{rad} > 0.7 m/s	V_{rad} > 1 m/s	V_{rad} > 1.5 m/s
number of observations	27103	7421	3383	842
$(Q_{spe})_{RIPLE} \in [0.75 \times (Q_{spe})_{La\ Robine} ; 1.25 \times (Q_{spe})_{La\ Robine}]$	15.7%	30.6%	38.4%	45.6%
$(Q_{spe})_{RIPLE} \in [0.5 \times (Q_{spe})_{La\ Robine} ; 1.5 \times (Q_{spe})_{La\ Robine}]$	29.8%	61.1%	77.7%	79.0%
$(Q_{spe})_{RIPLE} \in [0 \times (Q_{spe})_{La\ Robine} ; 2 \times (Q_{spe})_{La\ Robine}]$	89.0%	95.0%	94.6%	93.0%

To conclude, the comparison of specific discharges at the two stations needs to be put into perspective. First, the quality of the observed discharges at La Robine is not perfect, especially at high flow conditions, since few direct discharge measurements were available to build the stage-discharge rating curve. Second, it should be remembered that there is a 41% increase in the drained area between the 2 stations which means that the discharges at the two stations have to be rescaled to be compared. This is far from ideal, but there was no real alternative in this study. Therefore, it is still necessary to make comparisons of this type at other stations where reference data is available, in order to assess the velocimetric method presented in this study rigorously. Nevertheless, the results of this study show that the approach presented in this study is able to produce valuable continuous discharge time series during floods and more generally in medium to high flow conditions, despite the very frequent occurrence of bathymetric changes, given a limited investment of time and people in the field.

4.1.2 Uncertainty analysis

The results of the simplified uncertainty analysis applied to the velocimetric method are presented in Table 6. This table gives the relative error (in %) of each terms of uncertainty considered in this study. The dominant uncertainty terms are the two linear relations applied consecutively to transform V_{rad} into U_{mean}, the bathymetry of the "LSPIV cross-section" and the slope between the "radars cross-section" and the "LSPIV cross-section". Their relative error range between 7.1% and 12.6%. The relative uncertainty on Q which is calculated as the root square of the sum of the squares of the different terms of Table 6 is 20%. The four dominant terms of uncertainty listed above represent 83.2% of the uncertainty on Q and 98% of the relative uncertainty on Q considering the 6 sources shown in the Table 6.

Table 6 – Relative error (in %) of each terms of uncertainty considered in this study when applying the velocimetric method..

	$u'(V_{rad})$	$u'(V_{rad}, V_{s,max})_{rating}$	$u'(V_{s,max}, U_{mean})_{rating}$	u'(bathymetry)	$u'(H_{rad})$	u'(slope)
uncertainty (%)	4	12.6	7.1	10	0.01	8.7
relative weight of each uncertainty source (%)	9.4	32.8	15.6	17.2	0.0	17.6

This uncertainty analysis is simplified insofar as the uncertainty is considered to be constant whatever the discharge value. Referring to the previous section, it makes sense to follow this simplified analysis for situations where radar velocities are greater than 0.7 m/s, which corresponds to high flow conditions in this study. On the other hand, this simplified analysis does not really make sense for situations involving low radar velocities and low water levels. In such case, the uncertainty is largely underestimated.

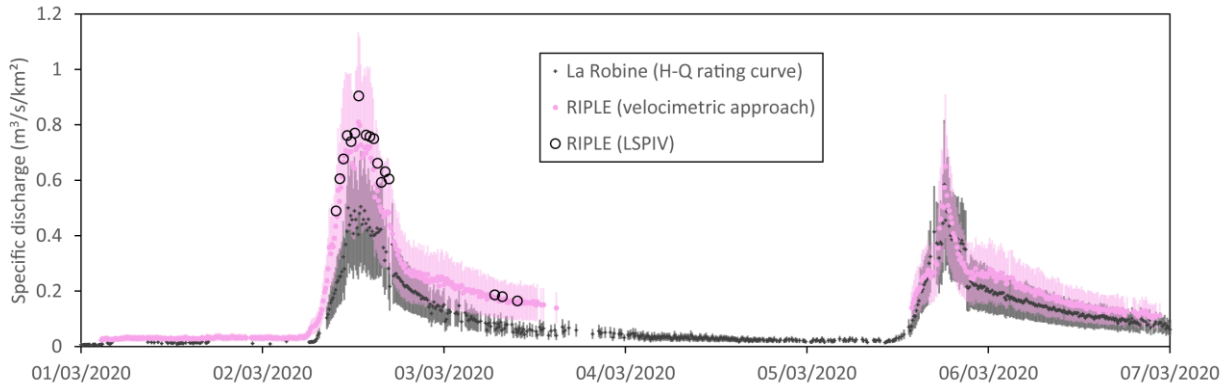

Figure 13 – Time series of specific discharge at the RIPLE station calculated using the approach presented in this study and at La Robine calculated using the stage-discharge rating curve for the period from 01/03/2020 to 07/03/2020. The 95% confidence intervals are shown in pink for data at RIPLE and in grey for data at La Robine. The values of specific discharge measured directly at RIPLE by the LSPIV method for the conditions reported in Table 2 are also shown.

The 95% confidence interval of Q is calculated as ± twice the value of the relative uncertainty on Q. Figure 13 exhibits the time series of specific discharge calculated using the approach presented in this study at the RIPLE station for the period from 01/03/2020 to 07/03/2020. On the same figure, the time series of specific discharge calculated at La Robine station using the stage-discharge rating curve is displayed. For this latter station, the relative uncertainty on Q considered by Navratil et al. (2011) in their global uncertainty analysis of suspended sediment monitoring was as high as 20%. Finally, the values of specific discharge calculated by the LSPIV method for the conditions reported in Table 2 (direct LSPIV measurements) are also shown in Figure 13. It can be checked that the values of specific discharge measured directly at RIPLE by the LSPIV method are within the confidence interval of the time series of specific discharge at RIPLE calculated using the approach presented in this study. Furthermore, it can be seen that the data of the two stations overlap during the two successive floods, except during the first phase of the rise of the first flood. At the end of the first flood and outside flood periods, the agreement between the data at the two stations decreases. This observation supports the previous conclusion which hinders the application of the method to low flow conditions.

4.2 Limitations and perspectives for improving the method

The method presented in this study makes it possible to produce reliable streamflow time series in a river prone to bathymetric shifts when no other method is available. As a result, the method has serious advantages to offer. However, the choice of the section to be instrumented must remain that of a hydrometer, as the conditions to be met are those for current meter gauging, i.e. reach of river as uniform as possible with quasi 1D velocities. Furthermore, it should be borne in mind that the method proposed in this study has yet to be validated with reference data in different environments. It should also be mentioned that this method does not allow a qualitative estimation discharge in low flow conditions, i.e. when radar velocities are below 0.7 m/s. This can pose problems for rivers located in areas of low slope. The method is also less effective for higher than bank-full discharges, as the position of the "y axis" is likely to change when flood plain is inundated.

In terms of uncertainty, we should recognize that our framework for computing the uncertainty is too simplistic, and has to be improved. It is clear that the relative error is largely underestimated for radar velocities lower than 0.7 m/s. However, it is important to bear in mind, that the idea that supports this research is to increase the spatial density of streamflow stations in the future, particularly in small rivers where it is impossible with current ressources to install more conventional hydrometric station (H-Q). In the end, it might be acceptable to have greater uncertainty on discharge estimation if, at the same time, the number of streamflow monitoring points increases spatially.

The perspective of this research would be to apply the method presented in this study in ungauged rivers and possibly in the absence of LSPIV discharge measurements. Indeed, the analysis of video sequences with the LSPIV method requires both time and expertise, which could hamper the multiplication of new stations of this type. It would be possible to automate the LSPIV method, but this would require a great deal of effort and the method would still have limitations in certain light conditions, as it is a passive method.

Our perspective is rather to try to be parsimonious and favours active instruments (i.e. radar or LiDAR). To do this, we propose in the future to position the H and V radars directly in the hydraulically suitable choosen section. In this study, this would have meant placing the radars directly above the “LSPIV cross section” using cables for instance, instead of placing them on the bridge ten meters upstream. This would eliminate two sources of error: the relation between H_{rad} to H_{LSPIV} and the relation between V_{rad} and V_{s,max_LSPIV}. Moreover, we propose to install the V radar directly at the “y axis”, assuming that the position of the “y axis” does not vary over time, except when the flood plain is inundated. By doing so, the relative uncertainty on Q would drop to 12.9% as two of the dominant terms of uncertainty would be removed in Table 6.

Different approaches can be considered for positioning the V radar at the “y axis” in the hydraulically suitable choosen section and assessing the the $U_{mean}/V_{\max}$ ratio. Fulton et al. (2020) propose to use at least one highly-resolved velocity gauging obtained by ADCP or current meter to identify the position of the "y axis" in the cross section and apply the entropy method for the vertical velocity profile at the “y axis” to predict also the $U_{mean}/V_{\max}$ ratio. Alternatively, if several highly-resolved velocity gaugings are available, Fulton et al. (2020) propose to calibrate the $U_{mean}/V_{\max}$ ratio with the historical pairs of U_{mean} and V_{max}. They mention that this second method is optimal. It also enables to improve the accuracy of the position of the “y axis” and therefore that of the V radar to be installed at that position. However, this approach still requires

a lot of human ressources and expertise in the field for highly-resolved velocity gaugings in different flow conditions. Moreover, there remains a doubt: it is not clear how Fulton et al. (2020) calculate U_{mean} from V_{rad} when the relation is established between the V_{max} and U_{mean}.

With the aim of being as parsimonious as possible while maintaining the quality of the estimates, we have tested in this study the possibility of predicting the position of the "y axis" and the ratio between $V_{s,max}$ and U_{mean} using theoretical methods, i.e. the Isovel model and the Q-Commander model. The results are promising, as these theoretical methods predict quite well the location of the “y axis” and the $U_{mean}/V_{s,\max}$ ratio based on limited information, i.e. the bathymetry of the cross-section and the bed roughness. These models still need to be evaluated in a larger number of rivers and environments where reference data are available. For the Isovel model, the results could certainly be further improved by considering a non-uniform roughness coefficient and by adjusting the exponent of the power law, set to 7 in this study. The impact on the quality of the discharge estimates should also be assessed when applying the "y axis" and the $U_{mean}/V_{s,\max}$ ratio predicted by these theoretical models. To realize this, it is necessary to have independent data of quality for the reference discharges.

Finally, one way of improving the method presented here would be to automate the detection of changes in the H_{rad} - V_{rad} scatter plot due to changes in the bathymetry by using machine-learning algorithms for example, and also to try to automate bathymetric surveys. (Gourley, 2017; Li et al., 2019; Stumpf et al., 2016) proposed methods to automate topographic surveys based on LiDAR and stereophotogrammetry, at least after the floods when the water level decreased sufficiently to expose to the air a large part of the cross-section. Such methods should be tested in future studies.

5 Conclusions

The application of the conventional method (stage-discharge rating curve) for monitoring of streamflow is not appropriate, or even not feasible, in rivers prone to frequent topographic shifts. This study proposes an effective and robust framework based on the index velocity method combined with non-contact instruments in order to provide continuous time series of streamflow in such rivers. The approach, which relies on water level and surface velocity radar monitoring, LSPIV discharge measurement and bathymetry surveys, is tested using a dataset of 2.5 years in a river of the southern French pre-Alps. By plotting the H_{rad} – V_{rad} scatter plot, the location in time of the bathymetric changes are easily detected - they all occur during floods - and six bathymetric periods are defined. For each bathymetric period, a relation between the water level and the wetted area of the cross-sectional profiles is built based on bathymetric surveys. A linear and proportional relation is then sought between the maximum surface velocity in the “LSPIV cross-section” called V_{s,max_LSPIV} and the cross-sectional velocity U_{mean_LSPIV}. The values of V_{s,max_LSPIV} are extracted for 69 video sequences recorded during floods. U_{mean} is obtained based on three different methods: (i) LSPIV discharge measurement; (ii) the Isovel model; (iii) the Q-Commander software developed by the Sommer company. The $U_{mean}/V_{s,\max\_LSPIV}$ ratio is respectively 0.686, 0.616 and 0.692 for the three methods listed previoulsy. Isovel and Q-Commander methods correctly predict the $U_{mean}/V_{s,\max\_LSPIV}$ ratio compared to the method calibrated with LSPIV discharge measurements (within a range of less than 10%), while they only rely on bathymetric, bed roughness and water level information as input. These are

therefore parsimonious methods that could prove useful in the future in the absence of highly resolved velocity gauging.

The location of the maximum velocity in the cross-section is also investigated in the study. The analysis of the LSPIV measurements show that the position of the "y axis" is relatively constant for all bathymetric periods and to a lesser extent when period 1 is also included, in spite of strong bathymetric changes. When the Isovel and Q-Commander models are applied, the mean value of the "y axis" represents a lateral shift to the right bank of 7% and 11% respectively, considering the width of the river at bank-full discharge, compared to the mean value obtained with the LSPIV measurements. These methods confirm the stability of the position of the "y axis" in presence of bathymetric changes.

Finally, discharge is calculated at each time step as the product of the cross-sectional velocity and the wetted area, to produce a time series of streamflow for the entire study period. The results are compared in terms of specific discharge with the data collected at an historical station located 2.5 km further upstream on the same river and presenting a stable H-Q rating curve. Data comparison is good when V_{rad} is above 0.7 m/s (NSE of 0.863, logNSE of 0.738, PBIAS of 2.9%) but much less good when V_{rad} is below 0.7 m/s (NSE of 0.580, logNSE of -0.084, PBIAS of 8.7%). The quality of the estimates increases as V_{rad} increases, since respectively 61.1% and 79% of the estimates are within the range ± 50% of the specific discharges at the historical station when V_{rad} is greater than 0.7 m/s and 1.5 m/s.

Acknowledgments

This work was supported by the French National Program (ANR) under the grant ANR-18-CE01-0019-01 (DEAR project). This research was also supported by ANR through the "Investment for Future – Excellency Equipment" project CRITEX with the reference ANR-11-EQPX-0011 and project TERRA FORMA with the reference ANR-21-ESRE-0014. The deployment of the RIPLE platform in the field was supported by the Labex OSUG@2020 (grant no. ANR10 LABX56) and the Institut National des Sciences de l'Univers (grant no. INSU/CNRS). The maintenance of the RIPLE platform and La Robine station was carried out by the technical service of the IGE.

Open Research

The data used to produce the results in this study are made available through two public repositories: one for the data of the RIPLE station (Nord, 2024) and another one for the data of the upstream station at La Robine sur Galabre (https://bdoh.irstea.fr/DRAIX/station/GALABRE). Please reach out to the corresponding author for further information.

References

United States Geological Survey. (2021). AreaComp Hydroacoustics [Software]. https://www.usgs.gov/software/areacomp-hydroacoustics-software

Ali, G., & Maghrebi, M. F. (2023). A robust approach for the derivation of rating curves using minimum gauging data. Journal of Hydrology, 623, 129609. https://doi.org/10.1016/j.jhydrol.2023.129609

Blake, J. R., & Packman, J. C. (2008). Identification and correction of water velocity measurement errors associated with ultrasonic Doppler flow monitoring. Water and Environment Journal, 22(3), 155–167. https://doi.org/10.1111/j.1747-6593.2007.00089.x

Botter, G., Carozzani, A., Peruzzo, P., & Durighetto, N. (2022). Steps dominate gas evasion from a mountain headwater stream. Nature Communications, 13(1), 7803. https://doi.org/10.1038/s41467-022-35552-3

Chen, C. L. (1991). Unified theory on power laws for flow resistance. Journal of Hydraulic Engineering, ASCE, 117(3), 371–389.

Chen, Y.-C., & Chiu, C.-L. (2004). A fast method of flood discharge estimation. Hydrological Processes, 18(9), 1671–1684. https://doi.org/10.1002/hyp.1476

Chiu C.-L. (1987). Entropy and probability concepts in hydraulics. Journal of Hydraulic Engineering, ASCE 113(5): 583–600.

1070 Chiu C.-L. (1988). Entropy and 2-D velocity distribution in open channels. Journal of Hydraulic
1071 Engineering, ASCE 114(7): 738–756.
1072 Chiu C.-L. (1991). Application of entropy concept in open-channel flow study. Journal of
1073 Hydraulic Engineering, ASCE 117(5): 615–628.
1074 Chiu C.-L., & Said AA. (1995). Maximum and mean velocities in open-channel flow. Journal of
1075 Hydraulic Engineering, ASCE 121(1): 26–35.
1076 Chiu, C.-L., & Chen, Y.-C. (2003). An efficient method of discharge estimation based on
1077 probability concept. Journal of Hydraulic Research, 41(6), 589–596.
1078 https://doi.org/10.1080/00221680309506891
1079 Chiu, C.-L., & Tung, N.-C. (2002). Maximum Velocity and Regularities in Open-Channel Flow.
1080 Journal of Hydraulic Engineering, 128(4), 390–398. https://doi.org/10.1061/(ASCE)0733-
1081 9429(2002)128:4(390)
1082 Coxon, G., Freer, J., Westerberg, I. K., Wagener, T., Woods, R., & Smith, P. J. (2015). A novel
1083 framework for discharge uncertainty quantification applied to 500 UK gauging stations. Water
1084 Resources Research, 51(7), 5531–5546. https://doi.org/10.1002/2014WR016532
1085 Darienzo, M., Renard, B., Le Coz, J., & Lang, M. (2021). Detection of Stage-Discharge Rating
1086 Shifts Using Gaugings: A Recursive Segmentation Procedure Accounting for Observational and
1087 Model Uncertainties. Water Resources Research, 57(4), e2020WR028607.
1088 https://doi.org/10.1029/2020WR028607
1089 Duvert, C., Butman, D. E., Marx, A., Ribolzi, O., & Hutley, L. B. (2018). CO2 evasion along
1090 streams driven by groundwater inputs and geomorphic controls. Nature Geoscience, 11(11),
1091 813–818. https://doi.org/10.1038/s41561-018-0245-y

1092 Eberts, S.M., Woodside, M.D., Landers, M.N., & Wagner, C.R. (2018). Monitoring the pulse of
1093 our Nation's rivers and streams—The U.S. Geological Survey streamgaging network. U.S.
1094 Geological Survey Fact Sheet 2018–3081, 2 p., https://doi.org/10.3133/fs20183081
1095 Esteves, M., Legout, C., Navratil, O., & Evrard, O. (2019). Medium term high frequency
1096 observation of discharges and suspended sediment in a Mediterranean mountainous catchment.
1097 Journal of Hydrology, 568, 562–574. https://doi.org/10.1016/j.jhydrol.2018.10.066
1098 Farina, G., Alvisi, S., Franchini, M., & Moramarco, T. (2014). Three Methods for Estimating the
1099 Entropy Parameter M Based on a Decreasing Number of Velocity Measurements in a River
1100 Cross-Section. Entropy, 16(5), 2512–2529. https://doi.org/10.3390/e16052512
1101 Fujita, I., Watanabe, H., & Tsubaki, R. (2007). Development of a non-intrusive and efficient
1102 flow monitoring technique: The space-time image velocimetry (STIV). International Journal of
1103 River Basin Management, 5(2), 105–114. https://doi.org/10.1080/15715124.2007.9635310
1104 Fulton, J. W., Mason, C. A., Eggleston, J. R., Nicotra, M. J., Chiu, C.-L., Henneberg, M. F., et al.
1105 (2020). Near-Field Remote Sensing of Surface Velocity and River Discharge Using Radars and
1106 the Probability Concept at 10 U.S. Geological Survey Streamgages. Remote Sensing, 12(8),
1107 1296. https://doi.org/10.3390/rs12081296
1108 Gonçalves, G. M. S., Bartels, G. K., Lima, L. S., Boeira, L. D. S., & Collares, G. L. (2023).
1109 Continuous discharge monitoring of the Mirim-São Gonçalo system by the index velocity rating
1110 curve method. Journal of Hydroinformatics, 25(1), 20–35.
1111 https://doi.org/10.2166/hydro.2023.045
1112 Gourley, J.J. (2017). In pursuit of flash flood data. Eos 98.
1113 https://doi.org/10.1029/2018EO079723

1114 Hauet, A., Kruger, A., Krajewski, W. F., Bradley, A., Muste, M., & Creutin, J. D. (2008).
1115 Experimental system for real-time discharge estimation using an image-based method. Journal of
1116 Hydrologic Engineering, 13, 105–110.
1117 Hauet, A., Morlot, T., & Daubagnan, L. (2018). Velocity profile and depth-averaged to surface
1118 velocity in natural streams: A review over alarge sample of rivers. E3S Web Conf., 40, 06015,
1119 https://doi.org/10.1051/e3sconf/20184006015
1120 Hayt, W. H. (1981). Engineering electromagnetics. 4 ed. New York: McGraw-Hill.
1121 Huang, Y., Chen, H., Liu, B., Huang, K., Wu, Z., & Yan, K. (2023). Radar Technology for River
1122 Flow Monitoring: Assessment of the Current Status and Future Challenges. Water, 15(10), 1904.
1123 https://doi.org/10.3390/w15101904
1124 ISO/IEC 98-3 (2010). Uncertainty of Measurement – Part 3: Guide to the Expression of
1125 Uncertainty in Measurement, ISO Edition, Geneva, Switzerland.
1126 Kästner, K., Hoitink, A. J. F., Torfs, P. J. J. F., Vermeulen, B., Ningsih, N. S., & Pramulya, M.
1127 (2018). Prerequisites for Accurate Monitoring of River Discharge Based on Fixed-Location
1128 Velocity Measurements. Water Resources Research, 54(2), 1058–1076.
1129 https://doi.org/10.1002/2017WR020990
1130 Kavousizadeh, A., & Ahmadi, A. (2018). High-performance approach for estimating stage-
1131 discharge curves in the open channels. Journal of Hydrology, 565, 197–213.
1132 https://doi.org/10.1016/j.jhydrol.2018.08.002
1133 Kiang, J. E., Gazoorian, C., McMillan, H., Coxon, G., Le Coz, J., Westerberg, I. K., et al. (2018).
1134 A Comparison of Methods for Streamflow Uncertainty Estimation. Water Resources Research,
1135 54(10), 7149–7176. https://doi.org/10.1029/2018WR022708

Le Coz, J., Hauet, A., Pierrefeu, G., Dramais, G., & Camenen, B. (2010). Performance of image-based velocimetry (LSPIV) applied to flash-flood discharge measurements in Mediterranean rivers. Journal of Hydrology, 394(1–2), 42–52. https://doi.org/10.1016/j.jhydrol.2010.05.049

Le Coz, J., Renard, B., Bonnifait, L., Branger, F., & Le Boursicaud, R. (2014). Combining hydraulic knowledge and uncertain gaugings in the estimation of hydrometric rating curves: A Bayesian approach. Journal of Hydrology, 509, 573–587. https://doi.org/10.1016/j.jhydrol.2013.11.016

Legout, C., Freche, G., Biron, R., Esteves, M., Navratil, O., Nord, G., et al. (2021). A critical zone observatory dedicated to suspended sediment transport: The meso-scale Galabre catchment (southern French Alps). Hydrological Processes, 35(3). https://doi.org/10.1002/hyp.14084

Levesque, V. A. & Oberg, K. A. (2012). Computing discharge using the index velocity method. U.S. Geological Survey Techniques and Methods 3–A23, https://doi.org/10.3133/tm3A23.

Li, W., Liao, Q., & Ran, Q. (2019). Stereo-imaging LSPIV (SI-LSPIV) for 3D water surface reconstruction and discharge measurement in mountain river flows. Journal of Hydrology, 578, 124099. https://doi.org/10.1016/j.jhydrol.2019.124099

Maghrebi, M. F. (2003). Discharge estimation in flumes using a new technique for the production of isovel contours. In Proceedings of International Conference on Civil and Environment Engineering, ICCEE, pp. 147–156.

Maghrebi, M. F., & Ball, J. E. (2006). New Method for Estimation of Discharge. Journal of Hydraulic Engineering, 132(10), 1044–1051. https://doi.org/10.1061/(ASCE)0733-9429(2006)132:10(1044)

Moramarco, T., & Singh, V. P. (2010). Formulation of the Entropy Parameter Based on Hydraulic and Geometric Characteristics of River Cross Sections. Journal of Hydrologic Engineering, 15(10), 852–858. https://doi.org/10.1061/(ASCE)HE.1943-5584.0000255

Muste, M., Fujita, I., & Hauet, A. (2008). Large-scale particle image velocimetry for measurements in riverine environments. Water Resources Research, 44, W00D19. doi:10.1029/2008WR006950.

Navratil, O., Esteves, M., Legout, C., Gratiot, N., Nemery, J., Willmore, S., & Grangeon, T. (2011). Global uncertainty analysis of suspended sediment monitoring using turbidimeter in a small mountainous river catchment. Journal of Hydrology, 398(3–4), 246–259. https://doi.org/10.1016/j.jhydrol.2010.12.025

Nord, G., Gallart, F., Gratiot, N., Soler, M., Reid, I., Vachtman, D., et al. (2014). Applicability of acoustic Doppler devices for flow velocity measurements and discharge estimation in flows with sediment transport. Journal of Hydrology, 509, 504–518. https://doi.org/10.1016/j.jhydrol.2013.11.020

Nord, G., Michielin, Y., Biron, R., Esteves, M., Freche, G., Geay, T., et al. (2020). An autonomous low-power instrument platform for monitoring water and solid discharges in mesoscale rivers. Geoscientific Instrumentation, Methods and Data Systems, 9(1), 41–67. https://doi.org/10.5194/gi-9-41-2020

Nord, G. (2024). Streamflow monitoring at high temporal resolution based on non-contact instruments in the Galabre river (Southern Pre-Alps, France) [Dataset]. Easy Data Earth. https://doi.org/10.57932/16ec87f0-b2db-42c6-bae5-8944c12f5d60

Pearce, S., Ljubičić, R., Peña-Haro, S., Perks, M., Tauro, F., Pizarro, A., et al. (2020). An Evaluation of Image Velocimetry Techniques under Low Flow Conditions and High Seeding

Densities Using Unmanned Aerial Systems. Remote Sensing, 12(2), 232. https://doi.org/10.3390/rs12020232

Rahman Khan, M., Gourley, J. J., Duarte, J. A., Vergara, H., Wasielewski, D., Ayral, P.-A., & Fulton, J. W. (2021). Uncertainty in remote sensing of streams using noncontact radars. Journal of Hydrology, 603, 126809. https://doi.org/10.1016/j.jhydrol.2021.126809

Rodríguez, E., Durand, M., & Frasson, R. P. D. M. (2020). Observing Rivers With Varying Spatial Scales. Water Resources Research, 56(9), e2019WR026476. https://doi.org/10.1029/2019WR026476

Shannon C.E. (1948). A mathematical theory of communication. The Bell System Technical Journal 27: 623–656.

Sommer Messtechnik GmbH (2013). Discharge calculation with the RQ-30. 4p.

Son, G., Kim, D., Kim, K., & Roh, Y. (2023). Performance of a Rectangular-Shaped Surface Velocity Radar for River Velocity Measurements. KSCE Journal of Civil Engineering. https://doi.org/10.1007/s12205-023-0272-0

Stumpf, A., Augereau, E., Delacourt, C., & Bonnier, J. (2016). Photogrammetric discharge monitoring of small tropical mountain rivers: A case study at Rivière des Pluies, Réunion Island: PHOTOGRAMMETRIC DISCHARGE MONITORING. Water Resources Research, 52(6), 4550–4570. https://doi.org/10.1002/2015WR018292

Welber, M., Le Coz, J., Laronne, J. B., Zolezzi, G., Zamler, D., Dramais, G., et al. (2016). Field assessment of noncontact stream gauging using portable surface velocity radars (SVR): FIELD ASSESSMENT OF PORTABLE SURFACE VELOCITY RADARS. Water Resources Research, 52(2), 1108–1126. https://doi.org/10.1002/2015WR017906

1202 Wright, S., & Parker, G. (2004). Flow resistance and suspended load in sand-bed rivers:
1203 Simplified stratification model. Journal of Hydraulic Engineering, 130(8), 796–805.
1204 https://doi.org/10.1061/(ASCE)0733-9429(2004)130:8(796)

1205

1206 **Appendix 1**. Time series of specific discharge at the RIPLE station (colour data) calculated
1207 using the velocimetric approach and at La Robine station calculated using the stage-discharge
1208 rating curve (black +).

1209

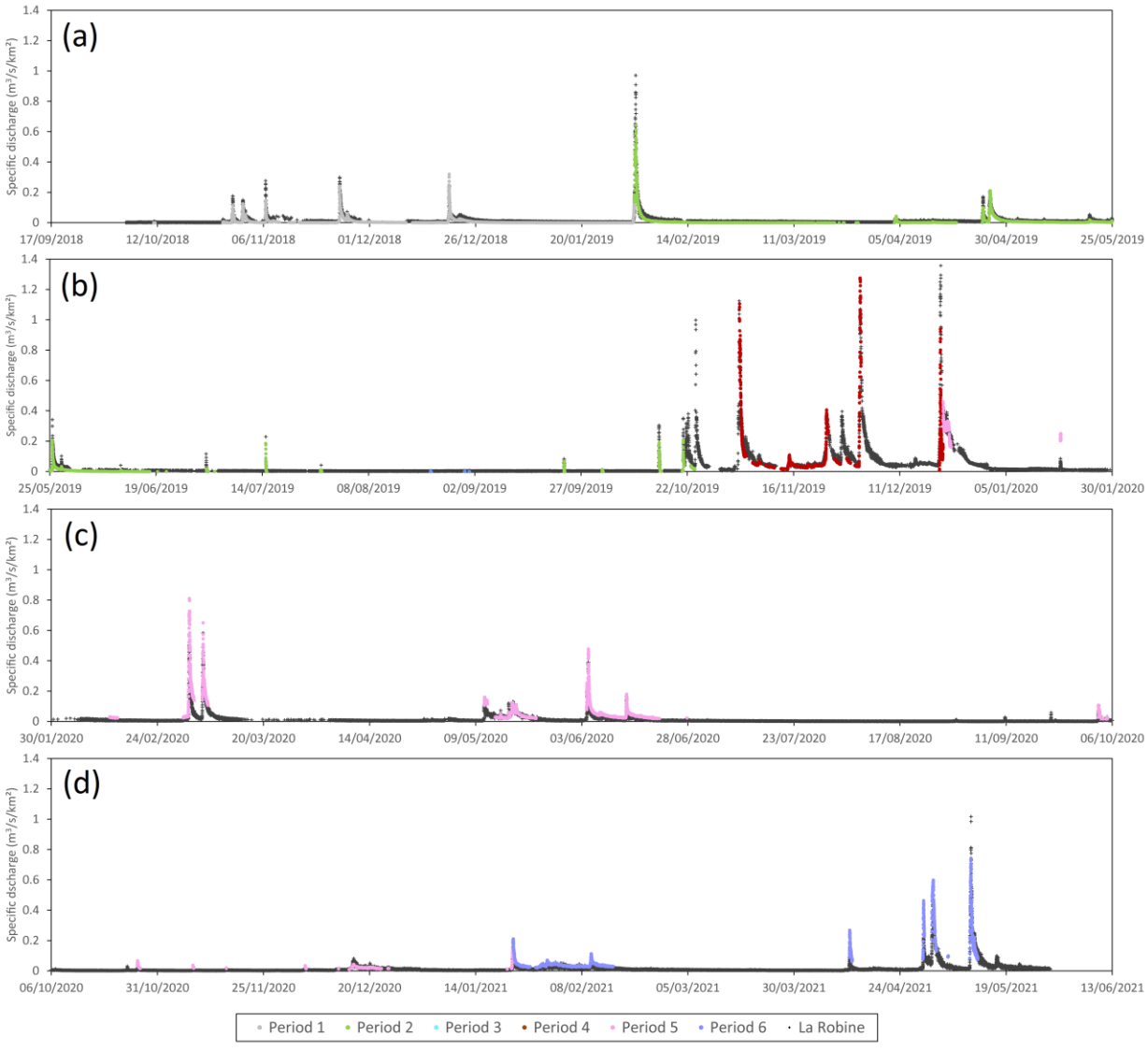

1210